

## Single Degenerate Models for Type Ia Supernovae Progenitor's Evolution and Nucleosynthesis Yields

Ken'ichi Nomoto, Shing-Chi Leung

Received: 8 March 2018 / Accepted: 28 March 2018

**Abstract** We review how the single degenerate models for Type Ia supernovae (SNe Ia) works. In the binary star system of a white dwarf (WD) and its non-degenerate companion star, the WD accretes either hydrogen-rich matter or helium and undergoes hydrogen and helium shell-burning. We summarize how the stability and non-linear behavior of such shell-burning depend on the accretion rate and the WD mass and how the WD blows strong wind. We identify the following evolutionary routes for the accreting WD to trigger a thermonuclear explosion. Typically, the accretion rate is quite high in the early stage and gradually decreases as a result of mass transfer. With decreasing rate, the WD evolves as follows: (1) At a rapid accretion phase, the WD increase its mass by stable H burning and blows a strong wind to keep its moderate radius. The wind is strong enough to strip a part of the companion star's envelope to control the accretion rate and forms circumstellar matter (CSM). If the WD explodes within CSM, it is observed as an "SN Ia-CSM". (X-rays emitted by the WD are absorbed by CSM.) (2) If the WD continues to accrete at a lower rate, the wind stops and an SN Ia is triggered under steady-stable H shell-burning, which is observed as a super-soft X-ray source: "SN Ia-SSXS". (3) If the accretion continues at a still lower rate, H shell-burning becomes unstable and many flashes recur. The WD undergoes recurrent nova (RN) whose mass ejection is smaller than the accreted matter. Then the WD evolves to an "SN Ia-RN". (4) If the companion is a He star (or a He WD), the accretion of He can trigger He and C double detonations at the sub-Chandrasekhar mass or the WD grows to the Chandrasekhar mass while producing and He-wind: "SN Ia-He CSM". (5) If the accreting WD rotates quite rapidly, the WD mass can exceed the Chandrasekhar mass of the spherical WD, which delays the trigger of an SN Ia. After angular momentum is lost from the WD, the (super-Chandra) WD contracts to become a delayed SN Ia. The companion star has become a

---

Ken'ichi Nomoto

Kavli Institute for the Physics and Mathematics of the Universe (WPI), The University of Tokyo, Kashiwa, Japan E-mail: nomoto@astron.s.u-tokyo.ac.jp

Shing-Chi Leung

Kavli Institute for the Physics and Mathematics of the Universe (WPI), The University of Tokyo, Kashiwa, Japan E-mail: shingchi.leung@ipmu.jp

He WD and CSM has disappeared: “SN Ia-He WD”. We update nucleosynthesis yields of the carbon deflagration model W7, delayed detonation model WDD2, and the sub-Chandrasekhar mass model to provide some constraints on the yields (such as Mn) from the comparison with the observations. We note the important metallicity effects on  $^{58}\text{Ni}$  and  $^{55}\text{Mn}$ .

**Keywords** Supernova · Progenitor · White Dwarf · Nucleosynthesis

## 1 Introduction

The thermonuclear explosion of a carbon+oxygen (C+O) white dwarf has successfully explained the basic observed features of Type Ia supernovae (SNe Ia) (e.g., Nomoto & Leung 2017; Leung and Nomoto 2018). Both the Chandrasekhar and the sub-Chandrasekhar mass models have been examined (e.g., Livio 2000). However, no clear observational indication exists as to how the white dwarf mass grows until carbon ignition, i.e., whether the white dwarf accretes H/He-rich matter from its binary companion [single-degenerate (SD) scenario] or whether two C+O white dwarfs merge [double-degenerate (DD) scenario] (e.g., Arnett 1969, 1996; Hillebrandt & Niemeyer 2000; Iben & Tutukov 1984; Ilkov & Soker 2012; Maoz, Mannicci & Nelemans 2014; Nomoto 1982a; Nomoto et al. 1994, 1997, 2000, 2009; Webbink 1984).

Here we focus on the possible evolutionary paths for the accreting white dwarf to increase its mass to the Chandrasekhar mass in the binary systems.

## 2 Hydrogen Shell-Burning in Accreting White Dwarfs

### 2.1 Effects of Mass Accretion on White Dwarfs

Isolated white dwarfs are simply cooling stars that eventually end up as invisible frigid stars. The white dwarf in a close binary system evolves differently because the companion star expands and transfers matter over to the white dwarf at a certain stage of its evolution. The mass accretion can *rejuvenate* the cold white dwarf (e.g., Nomoto and Sugimoto 1977), which could lead to a SNe Ia or accretion-induced collapse (AIC) in some cases.

The scenario that possibly brings a close binary system to a SN Ia or AIC is as follows: Initially the close binary system consists of two intermediate mass stars ( $M \lesssim 8 M_{\odot}$ ). As a result of Roche lobe overflow, the primary star of this system becomes a white dwarf composed of carbon and oxygen (C+O). When the secondary star evolves, it begins to transfer hydrogen-rich matter over to the white dwarf.

The mass accretion onto the white dwarf releases gravitational energy at the white dwarf surface. Most of the released energy is radiated away from the shocked region as UV and does not contribute much to heating the white dwarf interior. The continuing accretion compresses the previously accreted matter and releases gravitational energy in the interior. A part of this energy is transported to the surface and radiated away from the surface (*radiative cooling*) but the rest goes into thermal energy of the interior matter (*compressional heating*). Thus the interior temperature of the white dwarf is determined by the competition between

compressional heating and radiative cooling; i.e., the white dwarf is hotter if the mass accretion rate  $\dot{M}$  is larger, and vice versa (e.g., Nomoto 1982a,b).

## 2.2 Hydrogen Shell-Flashes

Hydrogen shell-burning is ignited when the mass of the accumulated hydrogen-rich matter reaches the ignition mass  $M_{\text{ig}} (= \Delta M_{\text{H}})$ . When  $M_{\text{ig}}$  is reached, the compressional heating due to accretion is just balanced with the cooling due to heat conduction (Nomoto, Nariai & Sugimoto 1979; Nomoto 1982a).  $M_{\text{ig}}$  is presented as contours on the  $M_{\text{WD}} - \dot{M} (= dM_{\text{H}}/dt)$  plane in Figure 1. For a given  $\dot{M}$ ,  $M_{\text{ig}}$  is smaller for a larger  $M_{\text{WD}}$  because of the smaller radius  $R$  and thus higher pressure for the same mass of accreted matter (see Equation 3 below). For a given  $M_{\text{WD}}$ ,  $M_{\text{ig}}$  is smaller for a higher  $\dot{M}$  because of the faster compressional heating and thus higher temperature of accreted matter.

The stability of the hydrogen burning shell in the accreting white dwarf is crucial for its evolution. Figure 1 summarizes the properties of hydrogen shell burning (Nomoto 1982a; Nomoto et al. 2007; Kato et al. 2014).

(1) The hydrogen shell burning is unstable to flash in the area below the solid line to show  $\dot{M}_{\text{stable}}$ . This stability line (dashed line) is approximately represented by Kato et al. (2014)

$$\dot{M}_{\text{stable}} = 4.17 \times 10^{-7} \left( \frac{M_{\text{WD}}}{M_{\odot}} - 0.53 \right) M_{\odot} \text{ yr}^{-1}. \quad (1)$$

(2) Above the dash-dotted line for  $\dot{M}_{\text{cr}} (= (dM/dt)_{\text{RH}})$ , the accreted matter is accumulated faster than consumed into He by H-shell burning. This critical accretion rate is represented as Kato et al. (2014)

$$\dot{M}_{\text{cr}} = 8.18 \times 10^{-7} \left( \frac{M_{\text{WD}}}{M_{\odot}} - 0.48 \right) M_{\odot} \text{ yr}^{-1}. \quad (2)$$

(3) For the region with  $\dot{M} > \dot{M}_{\text{cr}}$ , the accreted matter is piled up to form a red-giant size envelope (Nomoto, Nariai & Sugimoto 1979). This could lead to the formation of a common envelope and prevent further mass accretion onto the white dwarf. This problem has been resolved by the strong optically thick winds (Hachisu, Kato & Nomoto 1996; Hachisu et al. 1999; Hachisu, Kato & Nomoto 1999). If the wind is sufficiently strong, the white dwarf radius stays small enough to avoid the formation of a common envelope. Then steady hydrogen burning increases its mass at a rate  $\dot{M}_{\text{cr}}$  by blowing the extra mass away in a wind.

(4) In the area  $\dot{M}_{\text{stable}} < \dot{M} < \dot{M}_{\text{cr}}$ , accreting white dwarfs are thermally stable so that hydrogen burns steadily in the burning shell. Then the white dwarf mass increases at a rate of  $\dot{M}$ .

(5) For  $\dot{M} < \dot{M}_{\text{stable}}$ , the flash of hydrogen shell burning is stronger (weaker) for lower (higher)  $\dot{M}$  and thus for larger (smaller)  $M_{\text{ig}}$  and larger (smaller)  $M_{\text{WD}}$ .

The progress and the strength of the flashes are determined by two parameters ( $P^*$ ,  $\Omega^*$ ),

$$P^* = \frac{GM_{\text{WD}}M_{\text{ig}}}{4\pi R^4}, \quad \Omega^* = \frac{GM}{R}, \quad (3)$$

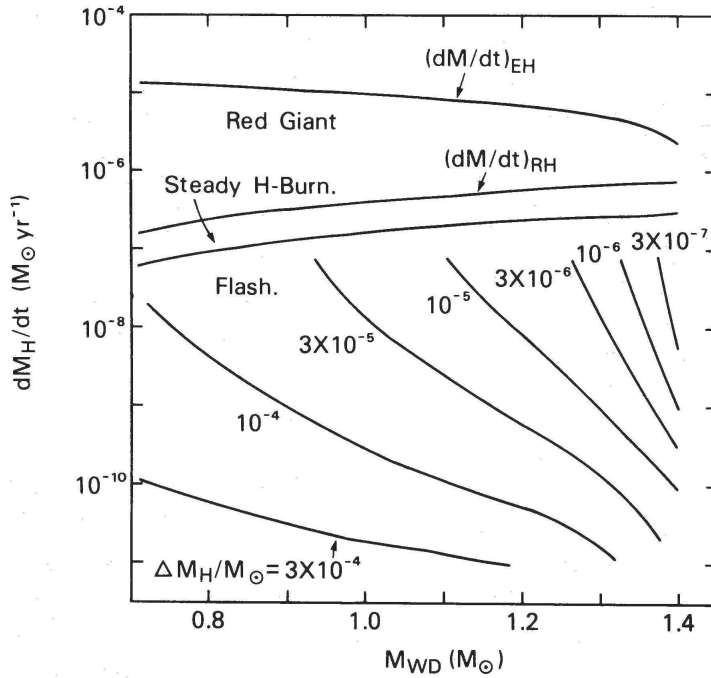


**Fig. 1** The properties of accreted hydrogen-rich materials as functions of  $M_{\text{WD}}$  and  $dM_{\text{H}}/dt$  (Nomoto 1982a). Hydrogen burning is stable in the region indicated by “Steady H-Burn” between the two lines of  $\dot{M}_{\text{stable}}$  in Equation 1 and  $\dot{M}_{\text{cr}} (=dM/dt)_{\text{RH}}$  in Equation 2 (Kato et al. 2014). In the region below  $\dot{M}_{\text{stable}}$ , hydrogen shell burning is thermally unstable, and the WD experiences shell flashes. Black solid lines indicate the hydrogen-ignition masses  $\Delta M_{\text{H}}$ , the values of which are shown beside each line. In the region above  $(dM/dt)_{\text{RH}}$  (and below the Eddington limit  $(dM/dt)_{\text{EH}}$ ), optically thick winds are accelerated, which prevents the formation of a red-giant size envelope with the piled-up accreted material as seen in Fig. 2 if no wind is included in the calculation Nomoto, Nariai & Sugimoto (1979). It has been found that optically thick wind are accelerated in this region, which prevents the formation of a red-giant (Hachisu, Kato & Nomoto 1996).

i.e., by the pressure and potential at the burning shell corresponding to completely *flat* configuration (Sugimoto & Fujimoto 1978; Sugimoto et al. 1979). A set of  $(P^*, \Omega^*)$  can be transformed into  $(M, M_{\text{ig}})$  since the radius at the burning shell is well approximated by the WD radius  $R$  which is smaller for larger  $M_{\text{WD}}$ .

Progress of the shell flash can be treated semi-analytically. Initially the temperature at the burning shell increases along  $P = P^*$ . As the nuclear energy is released, the pressure decreases as a result of expansion, which is described by  $P = fP^*$ . Here the flatness parameter  $f$  is unity for plane-parallel configuration and  $f < 1$  for more spherical configuration. This is expressed as

$$\frac{1}{f(V, N)} = \sum_{k=0}^{\infty} b_k, \quad b_0 = 1, \quad b_k = b_{k-1} \frac{k+3}{N+k+1} \frac{N+1}{V}, \quad V = r/H_p, \quad (4)$$

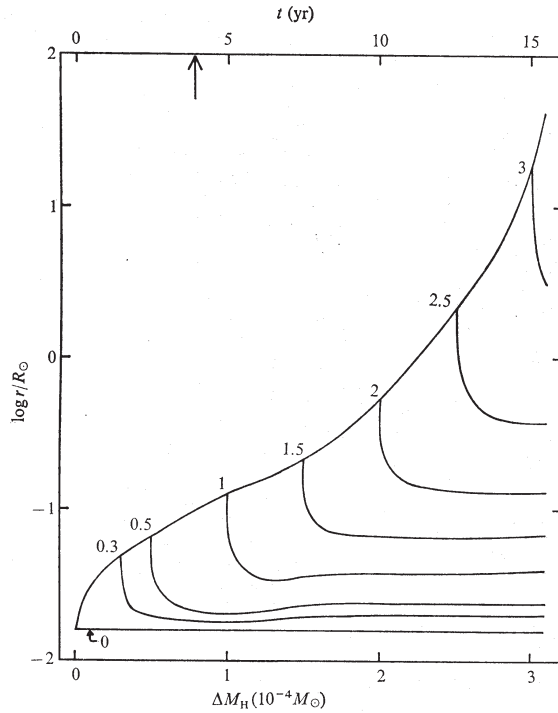


**Fig. 2** Increase in the radius of the accreting white dwarf upon the rapid accretion (Nomoto, Nariai & Sugimoto 1979).

where  $N$  and  $H_p$  denote the polytropic index for the convective envelope and the scale height of pressure, respectively (Sugimoto & Fujimoto 1978). As the specific entropy  $s$  in the hydrogen-burning shell increases,  $f$  decreases because of increasing  $H_p$ , i.e., expansion of the accreted envelope. This corresponds to the change in the configuration of the burning shell from plane parallel to spherical Sugimoto & Nomoto (1980).

Then the temperature reaches its maximum  $T_H^{\max}$ , which is higher for higher  $P^*$  and thus for higher  $M$  (smaller  $r$ ) and larger  $\Delta M_H$  (Eq. 3). Such a relation between  $T_H^{\max}$  and  $\Delta M_H$  for several  $M$  obtained from Equation 4 is shown in Figure 3 (Sugimoto et al. 1979). Results of some hydrodynamical calculations (X-mark) are in excellent agreement with the corresponding analytical predictions (filled circles). (Some discrepancies are likely to be caused by a coarse zoning in numerical calculations).

The results in Figures 1 and 3 show that generally smaller  $M$  and higher  $\dot{M}$  lead to a weaker flash because of the lower pressure at the flashing shell. For  $\dot{M} \sim 2 \times 10^{-7} - 10^{-8} M_\odot \text{ yr}^{-1}$ , the flash is so weak that the ejected mass is smaller than the mass which hydrogen burning converts into helium. Then the mass of the He layer can increase.

For  $\dot{M} \sim 10^{-9} - 10^{-8} M_\odot \text{ yr}^{-1}$ , the H-flash is stronger so that the mass of the He layer grows but at much lower rate.

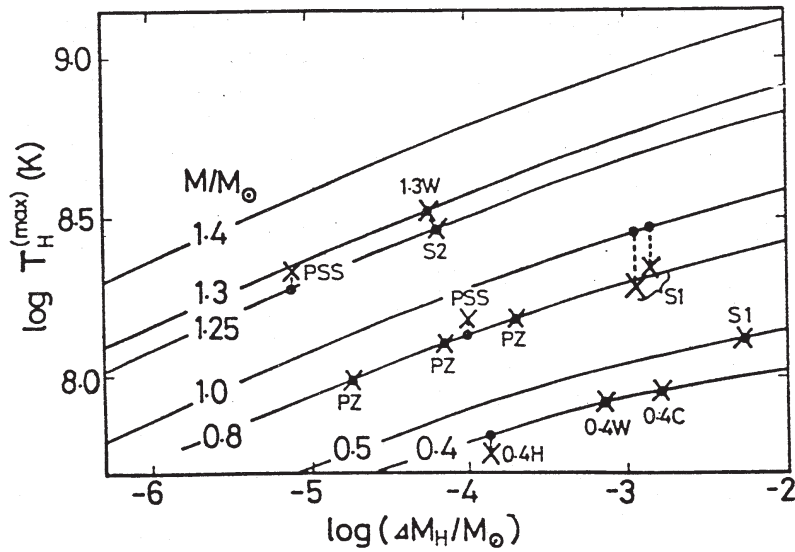


**Fig. 3** Maximum temperature attained during the hydrogen shell flash as a function of the accreted mass  $\Delta M_H$  and the white dwarf mass  $M$ . Analytical values (solid curves) are compared with those obtained by hydrodynamical calculations (X-mark) (see (Sugimoto et al. 1979) for details).

For slow accretion ( $\dot{M} \lesssim 1 \times 10^{-9} M_\odot \text{ yr}^{-1}$ ), hydrogen shell flash is strong enough to grow into a *nova* explosion, which leads to the ejection of most of the accreted matter from the white dwarf (e.g., Nariai, Nomoto & Sugimoto 1980). Moreover, a part of the original white dwarf matter is dredged up and lost in the outburst wind. Then  $M_{\text{WD}}$  decreases after the nova outburst. For these cases, the white dwarf does not become a *supernova* since its mass hardly grows. However, if the white dwarfs are close to the Chandrasekhar mass, novae could grow into AIC of SN Ia because the ejected mass from nova explosion is found to be significantly smaller than the accreted mass (Starrfield et al. 1991).

In these cases, the hydrogen flash recurs, and the recurrence period is proportional to  $M_{\text{ig}}/\dot{M}$ , which is shorter for higher  $\dot{M}$ . If the recurrence period is short, the flashes are observed as *recurrent novae*, which occurs in the upper-right region of Figure 1.

### 3 Evolution of Helium Accreting White Dwarfs

#### 3.1 Accretion of Helium

As discussed above, a thin He layer is produced and grows by H-burning for  $\dot{M} > 10^{-9} M_\odot \text{ yr}^{-1}$ . The He layer grows also by direct transfer of helium if the companion is a He star (e.g., Iben et al. 1987). Further evolution and final fates depend on the accretion rate of He and the mass of the C+O core  $M_{\text{CO}}$  as summarized in Figure 4.

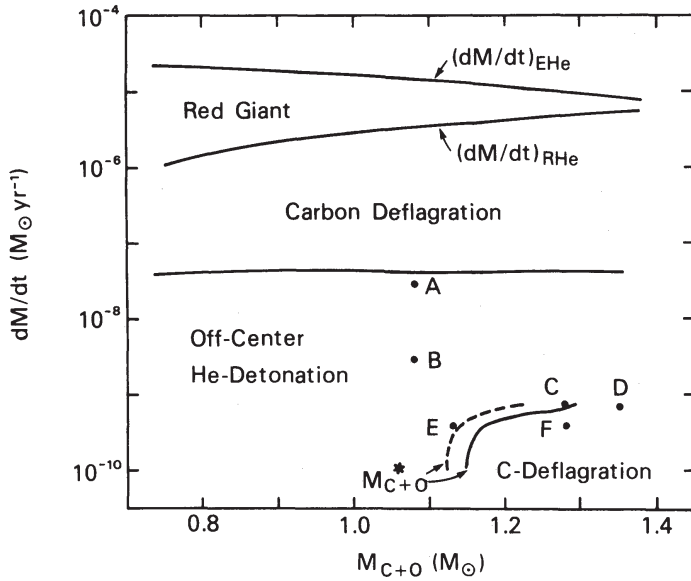


**Fig. 4** The properties of He accreting white dwarf as functions of  $M_{\text{WD}}$  and  $dM/dt$  (Nomoto 1982a). In the region above  $(dM/dt)_{\text{RHe}}$  (and below the Eddington limit  $(dM/dt)_{\text{EHe}}$ ), the accreted He envelope is extended to a red-giant size. In the region below  $\dot{M}_{\text{RHe}}$ , He shell burning is thermally unstable, and the WD experiences shell flashes.

When a certain mass  $\Delta M_{\text{He}}$  is accumulated, He shell-burning is ignited; the solid lines in Figure 5 show  $\Delta M_{\text{He}}$  as a function of  $\dot{M}$  and the white dwarf masses  $M$  (Kawai, Saio & Nomoto 1987). It is seen that  $\Delta M_{\text{He}}$  is larger for the slower mass-accumulation rate of the He layer  $\dot{M}_{\text{He}}$ .

If  $(dM/dt)_{\text{EHe}} \gtrsim \dot{M} \gtrsim (dM/dt)_{\text{RHe}}$  as in Figure 4, the accreted He envelope is extended to a red-giant size as seen in Figure 6. In the region below  $\dot{M}_{\text{RHe}}$ , He shell burning is thermally unstable, and the WD experiences shell flashes as discussed in the next subsection.

If the accretion of He is as slow as  $\dot{M} \lesssim 1 \times 10^{-9} M_{\odot} \text{yr}^{-1}$ , the accreted material is too cold to ignite He burning, so that the white dwarf mass increases. An exception is the case with  $M_{\text{CO}} \lesssim 1.1 M_{\odot}$  where pycnonuclear He burning is ignited at high enough densities (Nomoto 1982a,b).

### 3.2 Helium Shell-Flashes and Detonation

In the early stages of He shell-burning, the He envelope is electron-degenerate and geometrically almost flat. Because of the almost constant pressure at the bottom of the He-burning shell (Eq. 3), the temperature there increases and makes a He flash. Heated by He burning, the He envelope gradually expands, which decreases the pressure. Then, the temperature attains its maximum and starts decreasing.

The maximum temperature attained during the He shell-flash depends on  $\Delta M_{\text{He}}$  and  $M$  (Figure 7: Fujimoto & Sugimoto (1982)) as discussed for hydrogen

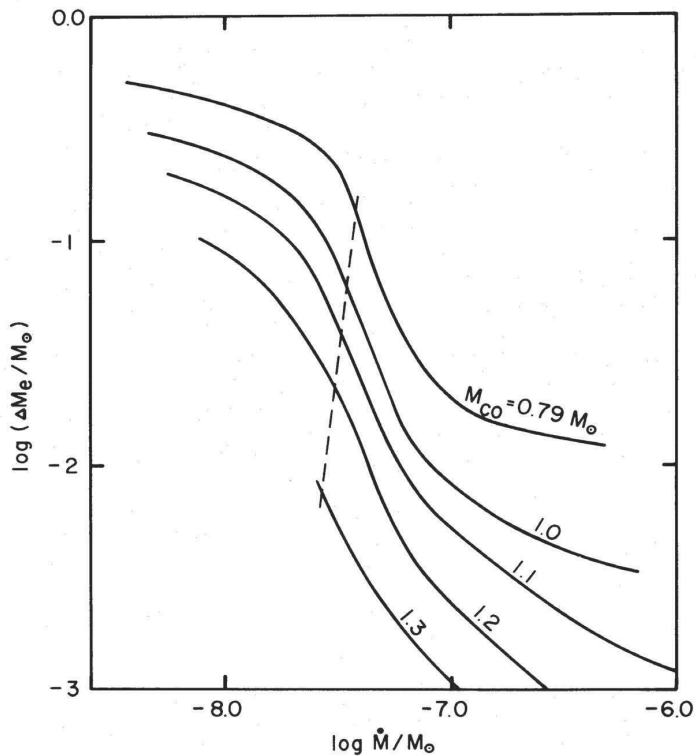


**Fig. 5** The mass of accreted He envelope,  $\Delta M_e$ , at the He ignition as a function of  $\dot{M}$  and the mass of underlying C+O core,  $M_{\text{CO}}$  (Kawai, Saio & Nomoto 1987).

in §2.2. The maximum temperature is higher for more massive WD and more massive envelope because of higher pressure. The strength depends on the He envelope mass  $M_{\text{env}}$ , thus depending mainly on  $\dot{M}$  as follows.

### 3.2.1 He Detonation

For  $\dot{M}_{\text{det}} \gtrsim \dot{M} \gtrsim 10^{-9} M_{\odot} \text{ yr}^{-1}$ , the He shell-flash is strong enough to initiate an off-center He detonation, which prevents the white dwarf mass from growing (e.g., Nomoto 1982b; Woosley, Taam & Weaver 1986). Here we adopt  $\dot{M}_{\text{det}} \sim 1 \times 10^{-8} M_{\odot} \text{ yr}^{-1}$ , since the  $^{14}\text{N}(e^-, \nu)^{14}\text{C}(\alpha, \gamma)^{18}\text{O}$  (NCO) reaction ignites weak He flashes (Hashimoto et al. 1986; Limongi and Tornambe 1991) if the mass fraction of CNO elements in the accreting material exceeds 0.005. For smaller CNO abundances, the NCO reaction is not effective and thus  $\dot{M}_{\text{det}} \sim 4 \times 10^{-8} M_{\odot} \text{ yr}^{-1}$  (Nomoto 1982a).

Two dimensional hydrodynamical simulations after the initiation of He detonation have been performed by several groups (e.g., Livne & Glasner (1991); Nomoto & Leung (2017) and references therein). The outcome is the off-center He-detonation, which develops into double detonation supernovae.



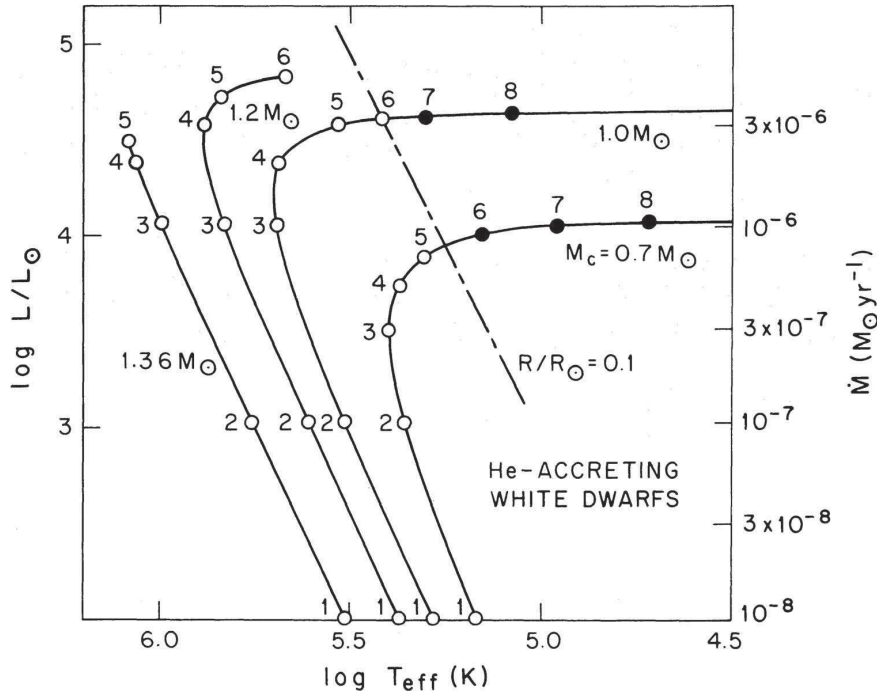


**Fig. 6** Locations of He-accreting steady state white dwarf models in the H-R diagram. The accretion rate is indicated on the right vertical axis. The solid lines connect models with the same C+O core mass. The thermally unstable and stable models are indicated by open and filled circles, respectively (Kawai, Saio & Nomoto 1988).

### 3.2.2 Recurring He Flashes

For intermediate accretion rates ( $3 \times 10^{-6} M_{\odot} \text{ yr}^{-1} \gtrsim \dot{M} \gtrsim 1 \times 10^{-8} M_{\odot} \text{ yr}^{-1}$ ), He shell-flashes are of moderate strength, thereby recurring many times to increase the white dwarf mass (Taam 1980; Fujimoto & Sugimoto 1982; Nomoto 1982b; Kato & Hachisu 2017). When the white dwarf mass becomes close to the Chandrasekhar mass, either thermonuclear explosion or collapse would occur.

Nucleosynthesis in such He shell-flashes has been calculated for various set of  $(M_{\text{WD}}, M_{\text{env}})$  (Nomoto, Kamiya & Nakasato 2013; Shen & Bildsten 2007). For higher maximum temperatures, heavier elements, such as  $^{28}\text{Si}$  and  $^{32}\text{S}$ , are synthesized. However, the maximum temperature is not high enough to produce  $^{40}\text{Ca}$ . After the peak, some amount of He remains unburned in the flash and burns into C+O during the stable He shell-burning. In this way, it is possible that an interesting amount of intermediate mass elements, including Si and S, already exist in the unburned C+O layer at  $M_r \geq 1.2M_{\odot}$ .

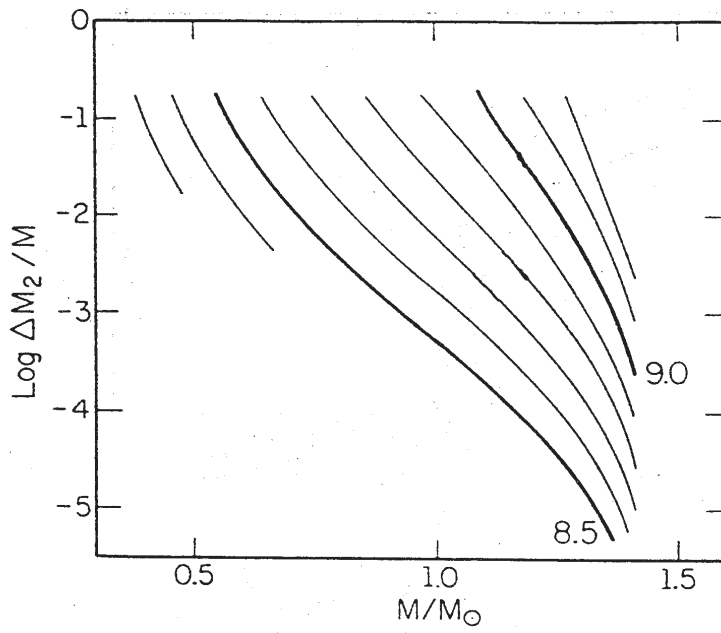


**Fig. 7** Maximum temperature  $\log T$  (K) attained during the He shell flash as a function of the accreted mass  $\Delta M_2$  and the white dwarf mass  $M$  (Fujimoto & Sugimoto 1982).

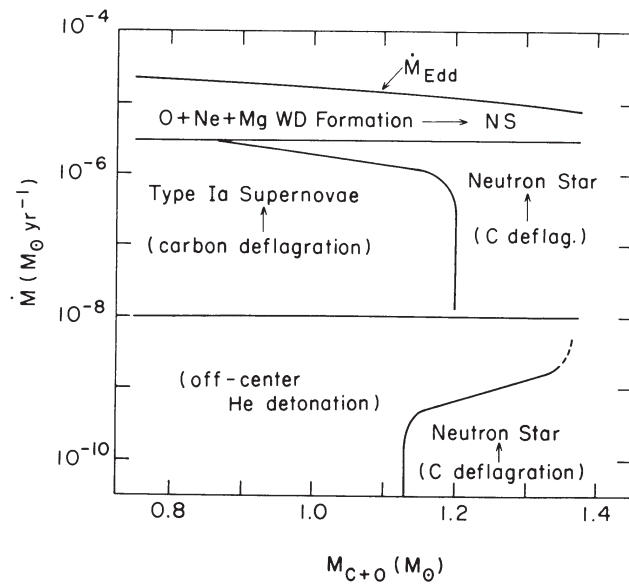


**Fig. 8** The final fate of C+O white dwarfs expected for their initial mass and accretion rate  $\dot{M}$  of C+O materials (Nomoto & Kondo 1991).

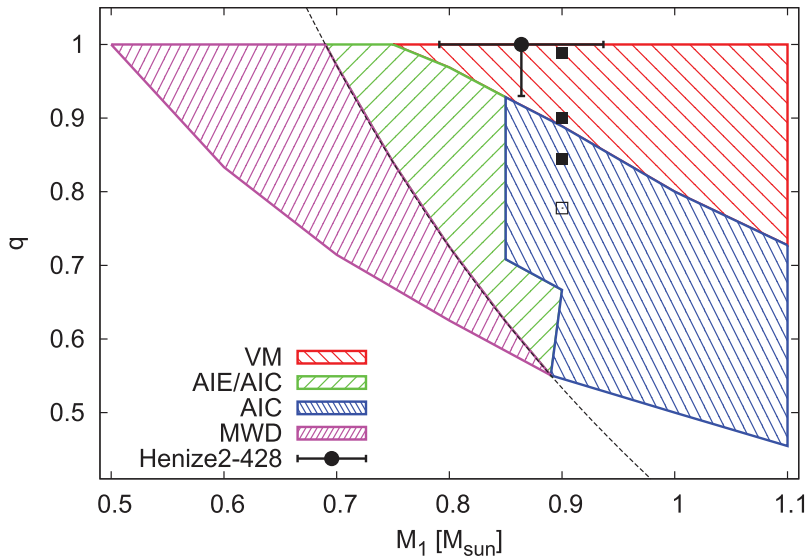


**Fig. 9** Final outcomes of our merger simulations in the mass ratio versus total mass diagram, i.e., violent merger, AIC (accretion-induced collapse), and AIE (accretion-induced explosion)/AIC (Sato et al. 2017). The black circle shows the possible ranges of the mass ratio and total mass of the central system of Henize 2-428 (Sato et al. 2016). The black squares denote the models calculated in Pakmor et al. (2011). Filled squares indicate the models which satisfied the detonation condition of Seitenzahl et al. (2009), while the open square indicates the model that does not.

### 3.3 Neutron Star Formation

For the C+O white dwarfs, whether they explode or collapse depends not only on  $\dot{M}$  but also on the initial mass  $M_{CO}$  as summarized in Figure 8. For  $M_{CO} < 1.2 M_{\odot}$ , substantial heat inflow from the surface layer into the central region ignites carbon at relatively low central density ( $\rho_c \sim 3 \times 10^9 \text{ g cm}^{-3}$ ) (Nomoto et al. 1984).

On the other hand, if the white dwarf is sufficiently massive and cold at the onset of accretion, the central region is compressed only adiabatically, thereby being cold (and solid) when carbon is ignited in the center of density as high as  $10^{10} \text{ g cm}^{-3}$ . C-burning at such high densities is likely to result in a collapse due to rapid electron capture in NSE (nuclear statistical equilibrium).

Neutron star formation is a possible outcome from high C-accretion rates as discussed in the next section on merging C+O WD (as indicated in Figure 8).

## 4 Merging of Double C+O White Dwarfs

Merging of double C+O white dwarfs is estimated to take place as frequently as SNe Ia (Iben & Tutukov 1984; Webbink 1984). Sato et al. (2017) performed SPH simulations of merging and summarized the final outcomes of mergers in the primary white dwarf mass ( $M_1$ ) versus the mass ratio of the two white dwarfs

( $q = M_2/M_1$ ) in Figure 9 as follows: (1) Violent Merger (VM): If the temperature of the shock-heated merged region becomes high enough, i.e., the timescale of the temperature rise due to C-burning becomes shorter than the dynamical timescale, C-detonation is generated which then triggers the central C-detonation at a relatively low central density as determined by  $M_1$ .

In Figure 9 (Sato et al. 2017), the black squares denote the models calculated in Pakmor et al. (2011). Filled squares indicate the models which satisfied the detonation condition of Seitenzahl et al. (2009), while the open square indicates the model that does not. (2) Accretion-induced collapse (AIC): If the temperature at the merged region leads to a stable off-center C-burning, C-flame propagates through the center to convert the C+O white dwarf into the O+Ne+Mg white dwarf, which would eventually collapse due to electron capture.

Such a C-ignition and subsequent flame propagation have been approximately simulated by spherical models. After the smaller mass white dwarf fills its Roche lobe, mass transfer of carbon onto the more massive white dwarf would be very rapid, which ignites off-center C-burning if  $\dot{M} \gtrsim 2.7 \times 10^{-6} M_\odot \text{ yr}^{-1}$  (Nomoto & Iben 1985). Subsequent flame propagation converts entire C+O into O+Ne+Mg (Saio & Nomoto 2004), which leads to collapse as induced by electron capture.

(3) Accretion-induced explosion (AIE): If the temperature after merging is too low to ignite carbon, the C+O white dwarf would increase its mass toward the Chandrasekhar mass (unless the accretion ignites off-center C burning) and leads to an SN Ia (Yoon et al. 2007).

(4) C+O white dwarf (MWD): If the total mass  $M_{\text{tot}} = M_1 + M_2$  of the two white dwarfs does not exceed the Chandrasekhar mass, the above cases (2) and (3) could not occur. Instead, the merger results in the formation of a single C+O white dwarf.

## 5 Four Cases of Pre-Explosion Configurations of Type Ia Supernovae

Based on the above properties of accretion-induced hydrogen shell burning, the binary system in the SD scenario evolves through stages (a)-(d) below (also shown in Figures 10a-d) (Hachisu, Kato & Nomoto 2008).

The more massive (primary) component of a binary evolves to a red giant star (with a helium core) or an AGB star (with a C+O core) and fills its Roche lobe. Mass transfer from the primary to the secondary begins and a common envelope is formed. After the first common envelope evolution, the separation shrinks and the primary component becomes a helium star or a C+O WD. The helium star evolves to a C+O WD after a large part of helium is exhausted by core-helium-burning. We eventually have a close pair of a C+O WD and a main-sequence (MS) star (Figure 10a).

Further evolution of the system depends on the binary parameters. Depending on at which stage SNe Ia are triggered, the SD scenario predicts the following four variations of SNe Ia.

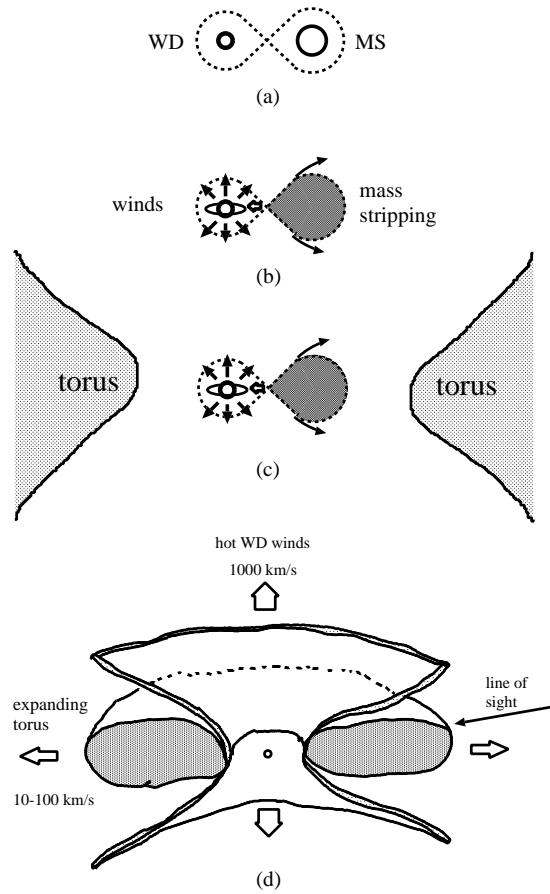


**Fig. 10** A schematic configuration of a binary evolution including mass-stripping effect (Hachisu, Kato & Nomoto 2008). (a) Here we start a pair of a C+O WD and a more massive main-sequence (MS) star with a separation of several to a few tens of solar radii. (b) When the secondary evolves to fill its Roche lobe, mass transfer onto the WD begins. The mass transfer rate exceeds a critical rate  $\dot{M}_{cr}$  for optically thick winds. Strong winds blow from the WD. (c) The hot wind from the WD hits the secondary and strips off its surface. (d) Such stripped-off material forms a massive circumstellar disk or torus and it gradually expands with an outward velocity of  $\sim 10 - 100 \text{ km s}^{-1}$ . The interaction between the WD wind and the circumstellar torus forms an hourglass structure. The WD mass increases up to  $M_{Ia} = 1.38 M_{\odot}$  and explodes as an SN Ia.

### 5.1 SNe Ia - Circumstellar Matter (CSM)

After the secondary evolves to fill its Roche lobe, the mass transfer to the WD begins. This mass transfer occurs on a thermal timescale because the secondary mass is more massive than the WD. The mass transfer rate exceeds  $\dot{M}_{cr}$  for the optically thick wind to blow from the WD (Hachisu, Kato & Nomoto 1996; Hachisu et al. 1999; Hachisu, Kato & Nomoto 1999) (Figure 10b).

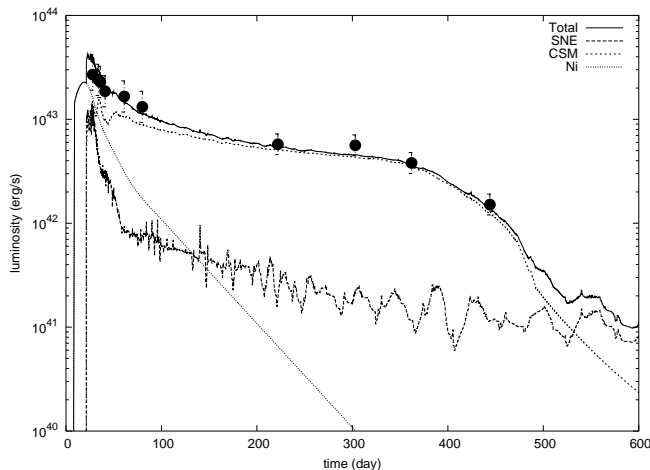


**Fig. 11** The observed light curve of SN Ia 2002ic (filled circles) and the calculated light curve with circumstellar interaction (Nomoto et al. 2005).

Optically thick winds from the WD collide with the secondary surface and strip off its surface layer. This mass-stripping attenuates the rate of mass transfer from the secondary to the WD, thus preventing the formation of a common envelope for a more massive secondary in the case with than in the case without this effect. Thus the mass-stripping effect widens the donor mass range of SN Ia progenitors (Figure 10c).

Such stripped-off matter forms a massive circumstellar torus on the orbital plane, which may be gradually expanding with an outward velocity of  $\sim 10 - 100 \text{ km s}^{-1}$  (Fig. 10d), because the escape velocity from the secondary surface to L3 point is  $v_{\text{esc}} \sim 100 \text{ km s}^{-1}$ . Subsequent interaction between the fast wind from the WD and the very slowly expanding circumbinary torus forms an hour-glass structure (Fig. 10c-d). When we observe the SN Ia from a high inclination angle such as denoted by “line of sight,” circumstellar matter can be detected as absorption lines like in SN 2006X.

This scenario predicts the presence of several types of circumstellar matter around the binary system, which are characterized various wind velocities  $v_w$ : (1) white dwarf winds with such high velocities as  $v_w \sim 1000 \text{ km s}^{-1}$ , (2) slow dense matter stripped off the companion star by the white dwarf wind, (3) slow wind matter ejected from a red-giant, and (4) moderate wind velocities blown from the main-sequence star.

The above features are supported by observations of the presence of circumstellar matter in some SNe Ia (Patat et al. 2007; Sternberg et al. 2011; Foley et al. 2012), and the detection of H in circumstellar-interaction type supernovae (Ia/IIn) such as SN 2002ic (Hamuy et al. 2003). SN 2002ic shows the typical spectral features of SNe Ia near maximum light, but also apparent hydrogen features that have been absent in ordinary SNe Ia. Its light curve has been reproduced by the model of interaction between the SN Ia ejecta and the H-rich circumstellar medium (Fig. 11) (Nomoto et al. 2005).

## 5.2 SNe Ia - Supersoft X-ray Sources

When the mass transfer rate decreases to the following range:  $\dot{M}_{\text{stable}} < \dot{M} < \dot{M}_{\text{cr}}$ , optically thick winds stop, and the WDs undergo steady H-burning. The WDs are observed as supersoft X-ray sources (SSXSs) until the SN Ia explosion. The stripped-off material forms circumstellar matter (CSM) but it has been dispersed too far to be detected immediately after the SN Ia explosion.

## 5.3 SNe Ia - Recurrent Novae

When the mass transfer rate from the secondary further decreases below the lowest rate of steady hydrogen burning, i.e.,  $\dot{M}_{\text{transfer}} < \dot{M}_{\text{stable}}$ , hydrogen shell burning is unstable to trigger a mild flashes, which recur many times in a short period as a recurrent nova (RN) (e.g., Nomoto et al. 2007). Its recurrent period is as short as  $\sim 1$  yr, which can be realized for high  $M$  and high  $\dot{M}$  as discussed in §2.2. These flashes burn a large enough fraction of accreted hydrogen to increase  $M$  to SNe Ia.

Observationally, PTF11kx (Dilday et al. 2012) provides strong evidences that the accreting white dwarf was a recurrent nova and the companion star was a red supergiant.

## 5.4 SNe Ia - He White Dwarf Remnants

In the rotating white dwarf scenario, which will be discussed in a later section (e.g., Benvenuto et al. 2015), ignition of central carbon burning is delayed in some cases due to the larger Chandrasekhar mass of the rotating white dwarfs than non-rotating white dwarfs. This delay time after the end of accretion up to the SN Ia explosion depends on the time scale of angular momentum loss from the C+O white dwarfs, and could be long enough for the companion star to evolve into a He white dwarf and for circumstellar materials to disperse. For such a delayed SN Ia, it would be difficult to detect a companion star or circumstellar matter.

## 5.5 Companion Stars in the SD Scenario

In SD scenario, SNe Ia can occur for a wide range of  $\dot{M}$ . The progenitor white dwarfs can grow their masses to the Chandrasekhar mass by accreting hydrogen-rich matter at a rate as high as  $\dot{M} \gtrsim 10^{-7} - 10^{-6} M_{\odot} \text{ yr}^{-1}$  (e.g., Hachisu, Kato & Nomoto 1996; Li & van den Heuvel 1997; Hachisu et al. 1999; Hachisu, Kato & Nomoto 1999; Langer et al. 2000; Han & Podsiadlowski 2004; Nomoto et al. 2000).

Two types of binary systems can provide such high accretion rates, i.e., (1) a white dwarf and a lobe-filling, more massive (up to  $\sim 7M_{\odot}$ ), slightly evolved main-sequence or sub-giant star (WD+MS), and (2) a white dwarf and a lobe-filling, less massive (typically  $\sim 1M_{\odot}$ ), red-giant (WD+RG) (Hachisu et al. 1999; Hachisu, Kato & Nomoto 1999). Figure 12 shows these two regions of (WD+MS) and (WD+RG) in the  $\log P - M_2$  (orbital period – secondary mass) plane (Hachisu, Kato & Nomoto 2008).

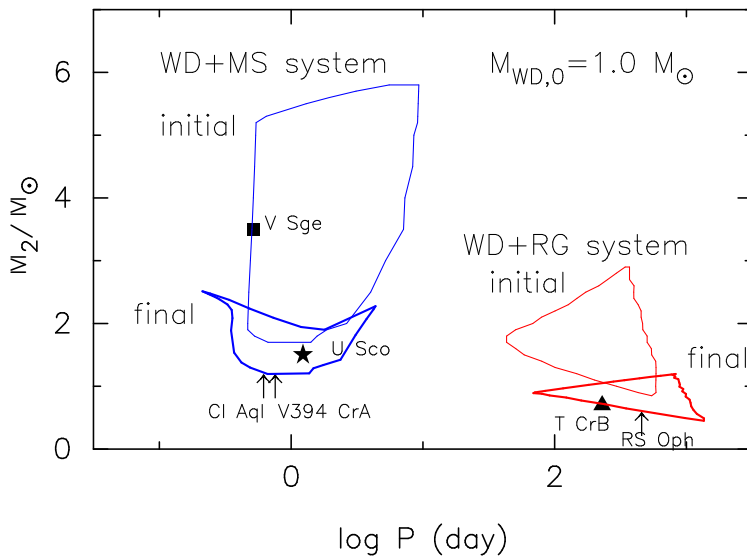


**Fig. 12** The regions that produce SNe Ia are plotted in the  $\log P - M_2$  (orbital period – secondary mass) plane for the (WD+MS) system (*left*) and the (WD+RG) system (*right*) (Hachisu, Kato & Nomoto 2008). Currently known positions of the recurrent novae and super-soft X-ray sources are indicated by a star mark ( $\star$ ) for U Sco, a triangle for T CrB, a square for V Sge, but by arrows for the other three recurrent novae, V394 CrA, CI Aql, and RS Oph. Two subclasses of the recurrent novae, the U Sco type and the RS Oph type, correspond to the WD + MS channel and the WD + RG channel of SNe Ia, respectively.

Here the metallicity of  $Z = 0.02$  and the initial white dwarf mass of  $M_{\text{WD},0} = 1.0 M_{\odot}$  are assumed. The initial system inside the region encircled by a thin solid line (labeled “initial”) increases its WD mass up to the critical mass ( $M_{\text{Ia}} = 1.38 M_{\odot}$ ) for the SN Ia explosion, the regions of which are encircled by a thick solid line (labeled “final”).

Note that the “initial” region of WD + MS systems extends up to such a massive ( $M_{2,0} \sim 5 - 6 M_{\odot}$ ) secondary, which consists of a very young population of SNe Ia with such a short delay time as  $t \lesssim 0.1$  Gyr. On the other hand, the WD + RG systems with a less massive RG ( $M_{2,0} \sim 0.9 - 1.0 M_{\odot}$ ) consist of a very old population of SNe Ia of  $t \gtrsim 10$  Gyr.

The delay time distribution (DTD) of SNe Ia on the basis of the above SD model (Fig. 12) has a featureless power law in good agreement with the observation (Hachisu, Kato & Nomoto 2008). This is because the mass of the secondary star of the SN Ia system ranges from  $M_{2,0} \sim 0.9$  to  $6 M_{\odot}$  due to the effects of the WD winds and the mass stripping. In our model, moreover, the number ratio of SNe Ia between the WD + MS component and the WD + RG component is  $r_{\text{MS/RG}} = 1.4$ . Such almost equal contributions of the two components help to yield a featureless power law.



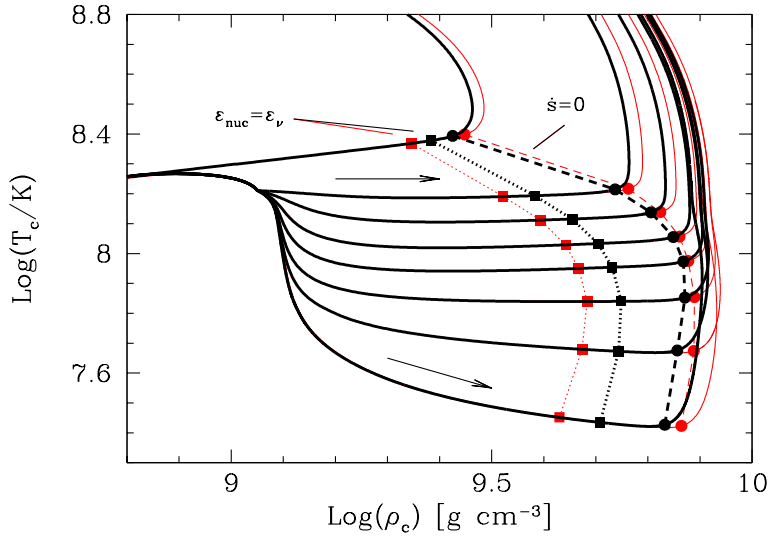


**Fig. 13** The evolutionary tracks of the center of the WD up to the onset of the hydrodynamical explosion (Benvenuto et al. 2015).  $\varepsilon_{\text{nuc}} = \varepsilon_{\nu}$  indicates the conditions at which neutrino losses equal nuclear energy release while  $\dot{S} = 0$  show the stages at which central entropy per baryon begins to increase. Thick black and thin red lines correspond to the treatments of screening given by Kitamura (2000) and Potekhin & Chabrier (2012), respectively. Arrows indicate the sense of the evolution.

## 5.6 Rotating White Dwarf

### 5.6.1 Uniform Rotation and Delayed Carbon Ignition

In the above sections, some observations that support the SD scenario are given. However, there has been no direct indication of the presence of companions, e.g., the lack of companion stars in images of SN 2011fe (Li et al. 2011) and some Type Ia supernova remnants (Schaefer & Pagnotta 2012). The rotating white dwarf scenario solves this missing-companion problem (Justham 2011; Di Stefano et al. 2011; Hachisu, Kato & Nomoto 2012; Benvenuto et al. 2015).

The rotating WD evolves as follows (Hachisu, Kato & Nomoto 2012; Benvenuto et al. 2015; Piersanti et al. 2003).

- (1) For certain ranges of binary parameters, the accretion rate ( $\dot{M}$ ) always exceeds  $10^{-7} M_{\odot} \text{ y}^{-1}$  so that the WD increases its mass until it undergoes “prompt” carbon ignition. The mass of the uniformly rotating WD at the carbon ignition,  $M_{\text{ig}}^{\text{R}}$ , is larger for smaller  $\dot{M}$ . For  $\dot{M} = 10^{-7} M_{\odot} \text{ y}^{-1}$ ,  $M_{\text{ig}}^{\text{R}} = 1.43 M_{\odot}$ , which is the largest mass because nova-like hydrogen flashes prevent the the WD mass from growing for the lower  $\dot{M}$ . Because of the centrifugal force in the rotating WD,  $M_{\text{ig}}^{\text{R}} = 1.43 M_{\odot}$  is larger than  $M_{\text{ig}}^{\text{NR}} = 1.38 M_{\odot}$  (Nomoto et al. 1984).
- (2) For adjacent ranges of binary parameters, the mass of the rotating WD exceeds  $M_{\text{ig}}^{\text{NR}} = 1.38 M_{\odot}$  but does not reach  $M_{\text{ig}}^{\text{R}} = 1.43 M_{\odot}$  because of the decreasing

accretion rate. After the accretion rate falls off, the WD undergoes the angular momentum-loss (J-loss) evolution. The exact mechanism and the time scale of the J-loss are highly uncertain, although the magneto-dipole braking WD is responsible. J-loss induces the contraction of the WD, which leads to the “delayed” carbon ignition after the “delay” time due to neutrino and radiative cooling.

Figure 13 shows the evolution of the center of the WD since before the end of accretion up to the onset of the hydrodynamical stage (Benvenuto et al. 2015). The upper-most line corresponds to the case (1) evolution that leads to the “prompt” carbon ignition. Below that, the lines from upper to lower correspond to the evolutions with increasing J-loss timescale ( $\tau_J = 1, 3, 10, 30, 100, 300,$  and  $1000$  Myr, respectively), that lead to the “delayed” carbon ignition.

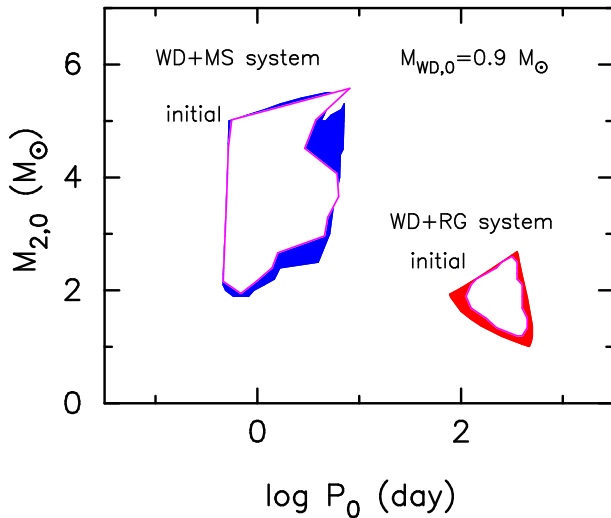


**Fig. 14** The outcome of the binary evolution of the WD + companion star systems is shown in the parameter space of the initial orbital period  $P$  and the companion mass  $M_2$  for the initial WD mass of  $0.9M_\odot$  (Benvenuto et al. 2015). The mass  $M$  of the WD starting from the “painted” region reaches  $1.38 M_\odot < M < 1.43 M_\odot$  (delayed carbon ignition), while the systems starting from the blank region encircled by the solid line reach  $M = 1.43 M_\odot$  (prompt carbon ignition).

In what binary systems ( $P$  and  $M_2$ ) does a uniformly rotating WD undergo the delayed carbon ignition? The result for the initial WD masses of  $0.9M_\odot$  is shown in Figure 14. Here the binary systems starting from the “painted” region of the ( $P - M_2$ ) plane reach  $1.38 M_\odot < M < 1.43 M_\odot$ , while the systems starting from the blank region encircled by the solid line reach  $M = 1.43 M_\odot$ . The occurrence frequency of the delayed carbon ignition would roughly be one-third of the total frequency of the carbon ignition.

For the values of  $\tau_J$  considered here, the WD spends enough time to undergo SN Ia explosion for the donor star to evolve to a structure completely different from the one it had when acted as a donor. For the red-giant donor, its H-rich envelope would be lost as a result of H-shell burning and mass loss so that it would become a He WD in  $\sim 10$  Myr. For the main sequence donor, it would also

evolve to become a low mass He WD in 1 Myr, a hot He WD in 10 Myr, and a cold He WD in 1000 Myr (Di Stefano et al. 2011). So, the J-losses should delay the explosion long enough for the former donor to be undetectable. Therefore, this scenario provides a way to account for the failure in detecting companions to SNe Ia.

Such He white dwarf companions would be faint enough not to be seen before or after the Type Ia supernova explosion. This new single-degenerate scenario can explain in a unified manner why no signatures of the companion star are seen in some Type Ia supernovae, whereas some Type Ia supernovae indicate the presence of the companion star.

### 5.6.2 Differential Rotation and Super-Chandra SNe Ia

If the accretion leads to non-uniform, differentially rotating WDs, carbon ignition occurs at super-Chandrasekhar masses (Hachisu et al. 2012). The WD mass can increase by accretion up to 2.3 (2.7)  $M_{\odot}$  from the initial value of 1.1 (1.2)  $M_{\odot}$ , being consistent with high luminosity SNe Ia such as SN 2003fg, SN 2006gz, SN 2007if, and SN 2009dc (Kamiya et al. 2012). Such very bright super-Chandrasekhar mass SNe Ia are suggested to be born in a low metallicity environment.

## 6 Nucleosynthesis Yields

To distinguish the progenitor scenarios between SD and DD, or the Chandrasekhar mass and sub-Chandrasekhar mass models, comparisons of nucleosynthesis features between these scenarios/models predictions (e.g. Thielemann (1986); Nomoto, Kamiya & Nakasato (2013)).

To provide the basis to obtain nucleosynthesis constraints, we recalculate nucleosynthesis yields of 1D explosion models with new nuclear reaction rates and weak interaction rates (Leung and Nomoto (2018); see also Mori et al. (2016)).

### 6.1 Yields from Chandrasekhar Mass White Dwarfs

We renew the nucleosynthesis yields of 1D models W7 and WDD2 Nomoto et al. (1984); Iwamoto et al. (1999). In these Chandrasekhar mass models, carbon burning ignited in the central region is unstable to flash because of strong electron degeneracy and release a large amount of nuclear energy explosively. However, the central density is too high and thus the shock wave is too weak to initiate a carbon detonation (because of temperature-insensitive pressure of strongly degenerate electrons).

Then the explosive thermonuclear burning front propagates outward as a convective deflagration wave (subsonic flame) (Nomoto, Sugimoto & Neo 1976). Rayleigh-Taylor instabilities at the flame front cause the development of turbulent eddies, which increase the flame surface area, enhancing the net burning rate and accelerating the flame. In the 1D convective deflagration model W7 (Nomoto et al. 1984), the flame speed is prescribed by time-dependent mixing-length theory with the mixing length being 0.7 of the pressure scale height. (In the central region, the mixing length is assumed to be equal to the radial distance from the center.)

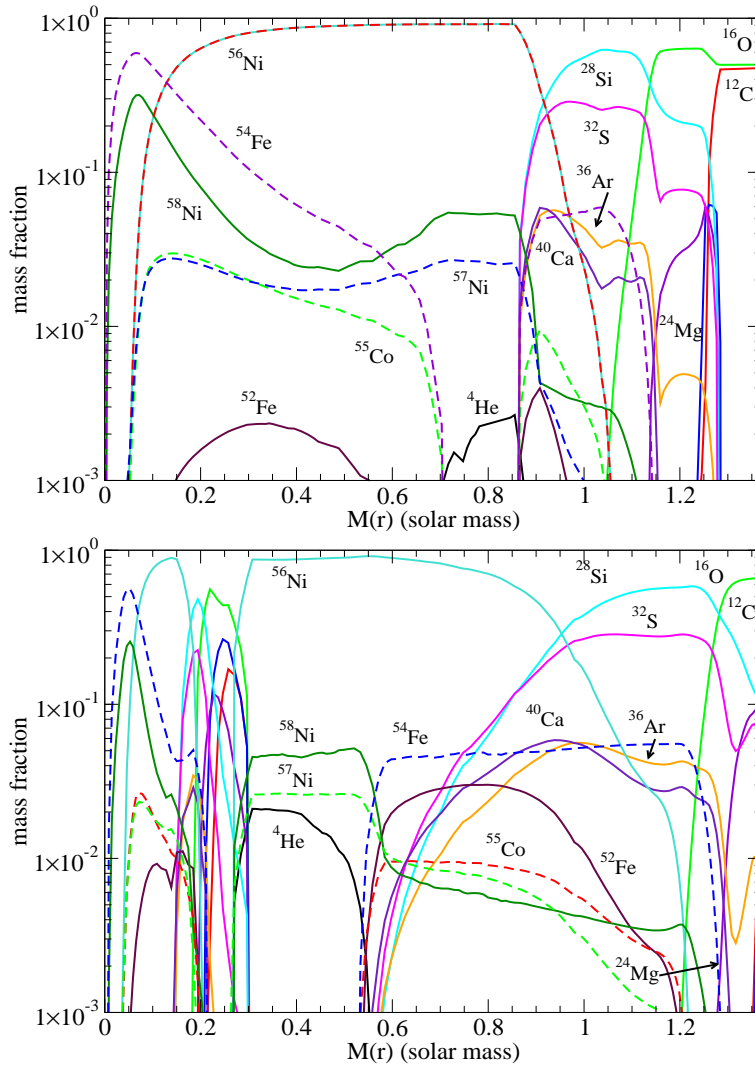


**Fig. 15** (upper panel) Mass fraction against  $M_r$  for the W7 model using the new nuclear reaction rates and electron capture rates (Leung and Nomoto 2018). (lower panel) Same as the upper panel, but for the WDD2 model.

In some cases the deflagration may undergo “deflagration to detonation transition (DDT)” (Khokhlov 1991). In the 1D DDT model WDD2 (Iwamoto et al. 1999), DDT is assumed to occur when the density at the flame front decreases to  $2 \times 10^7 \text{ g cm}^{-3}$ . Such a turbulent nature of the flame propagation has been studied in multi-dimensional simulations (e.g., Leung, Chu & Lin 2015a; Leung, Chu & Lin. 2015b; Nomoto & Leung 2017; Leung and Nomoto 2018).

In Figure 15 we plot the abundance distributions (mass fractions of main species) of W7 (upper panel) and WDD2 (lower panel). In the central region of these models, the temperature behind the deflagration wave exceeds  $\sim 5 \times 10^9 \text{ K}$ ,

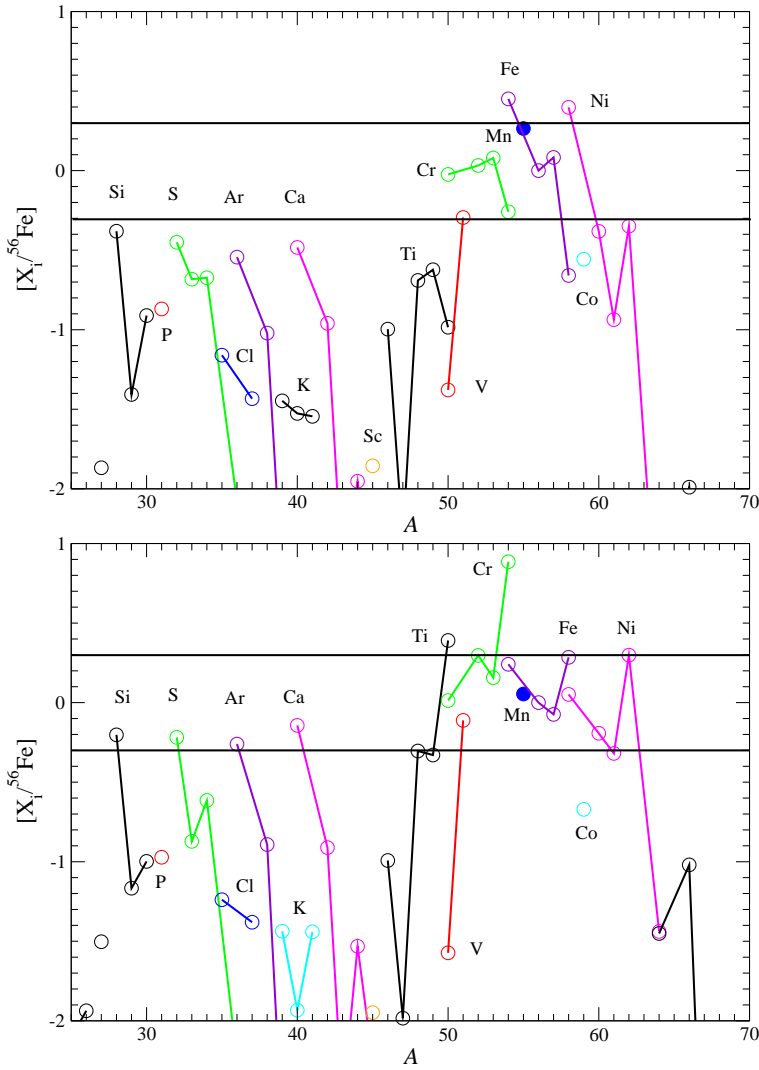


**Fig. 16** (upper panel)  $[X_i/^{56}\text{Fe}]$  for the W7 model using the new nuclear reaction rates and electron capture rates (Leung and Nomoto 2018). (lower panel) Same as the upper panel, but for the WDD2 model. The corresponding yielded mass for the stable and radioactive isotopes are also listed in Tables 1, 2 and 3. (*Remark:* The two figures are replaced due to the updated table.)

so that the reactions are rapid enough (compared with the expansion timescale) to realize nuclear statistical equilibrium (NSE). The central densities of the WDs are so high ( $\sim 3 \times 10^9 \text{ g cm}^{-3}$ ) that electron capture reduces the electron mole fraction,  $Y_e$ , that is the number of electrons per baryon. Then a significant amount of neutron-rich species, such as  $^{58}\text{Ni}$ ,  $^{57}\text{Ni}$ ,  $^{56}\text{Fe}$ ,  $^{54}\text{Fe}$ , and  $^{55}\text{Co}$  (which decays to  $^{55}\text{M}$ ), are synthesized.

In W7,  $0.65 M_\odot$   $^{56}\text{Ni}$  are produced. The surrounding layers at  $M_r > 0.8 M_\odot$  gradually expand during the subsonic flame propagation, so that the densities and

temperatures get lower. As a result, explosive burning produces the intermediate mass elements  $^{28}\text{Si}$ ,  $^{32}\text{S}$ ,  $^{36}\text{Ar}$  and  $^{40}\text{Ca}$  due to lower peak temperatures than in the central region. Beyond  $M_r = 1.2M_\odot$  explosive O-burning is slow so that  $^{16}\text{O}$  is dominant. The deflagration wave does not reach beyond  $m(r) = 1.3M_\odot$  so that  $^{12}\text{C}$  and  $^{16}\text{O}$  remain unburned.

In WDD2, the deflagration speed is assumed to be slower than W7 and undergoes the deflagration-detonation-transition (DDT). Then the chemical profile shows a two-layer structure. In the innermost  $0.3 M_\odot$  where the materials are burnt by deflagration, dominant products are similar to W7. After DDT, dominant nucleosynthesis products are somewhat neutron-rich Fe-peak species (e.g.,  $^{58}\text{Ni}$ ,  $^{57}\text{Ni}$ ,  $^{56}\text{Ni}$ ) at  $M_r < 1M_\odot$ , intermediate mass elements (e.g.  $^{28}\text{Si}$  and  $^{32}\text{S}$ ) at  $1M_\odot < M_r < 1.3M_\odot$ , and  $^{16}\text{O}$  in the outermost layers. There is almost no unburnt  $^{12}\text{C}$ , showing the detonation wave can sweep the whole white dwarf before it quenches. The total amount of  $^{56}\text{Ni}$  is  $0.67 M_\odot$  (Iwamoto et al. 1999).

Figures 16 show  $[X_i/^{56}\text{Fe}]$  of the stable isotopes from C to Zn for W7 (upper panel) and WDD2 (lower panel). The detailed abundance ratios with respect to  $^{56}\text{Fe}$  depend on the convective flame speed and the central densities, and also the weak reaction rates. In the old W7 and WDD2, electron capture rates by Fuller, Fowler, & Newman (1982) were used. In Figure 16, the most updated weak reaction rates are applied for electron capture Langanke et al. (2001). The ratio of  $[^{58}\text{Ni}/^{56}\text{Fe}]$  is reduced from  $\sim 0.6$  in the old W7 to  $\sim 0.3$  in the new W7, although some neutron-rich species are still enhanced relative to  $^{56}\text{Fe}$ .

For W7, the metallicity dependent yields are calculated for the initial mass fraction of  $^{22}\text{Ne}$  in the C+O white dwarfs  $X(^{22}\text{Ne}) = 0.025, 0.014,$  and  $0.0025$  as given in (Yield Table 2018). The metallicity effects are not so large in contrast to the sub-Chandrasekhar mass models (see next section) because synthesis of neutron-rich species is mostly due to electron capture in the NSE region rather than the initial metallicity  $X(^{22}\text{Ne})$ .

## 6.2 Yields from sub-Chandrasekhar Mass White Dwarf Models

There exist possible cases where an explosive carbon ignition occurs in sub-Chandrasekhar mass C+O white dwarfs. In the single degenerate model, an off-center He detonation is induced by relatively slow accretion of He as seen in Figure 5. In some cases, a resulting shock wave does not induce an immediate off-center C-detonation but propagates toward the central region and increase its strength because of decreasing area at the shock front. Then the shock wave becomes strong enough to ignite explosive carbon burning which forms a detonation wave (e.g., Livne 1990; Woosley & Weaver 1994). In the merging model, a merging of double white dwarfs ignites an off-center carbon flash that produces a shock wave. The shock wave propagates through the center and induces C-detonation (e.g., Pakmor et al. 2011).

Shigeyama et al. (1992) and Nomoto et al. (1994) calculated explosive nucleosynthesis in such sub-Chandrasekhar mass models by artificially inducing a C-detonation at center of the white dwarf. We have calculated similar sub-Chandrasekhar mass models by updating nuclear reaction rates. Figures 17 show the abundance distributions of the  $M = 1.0 M_\odot$  white dwarf models for the solar metallicity

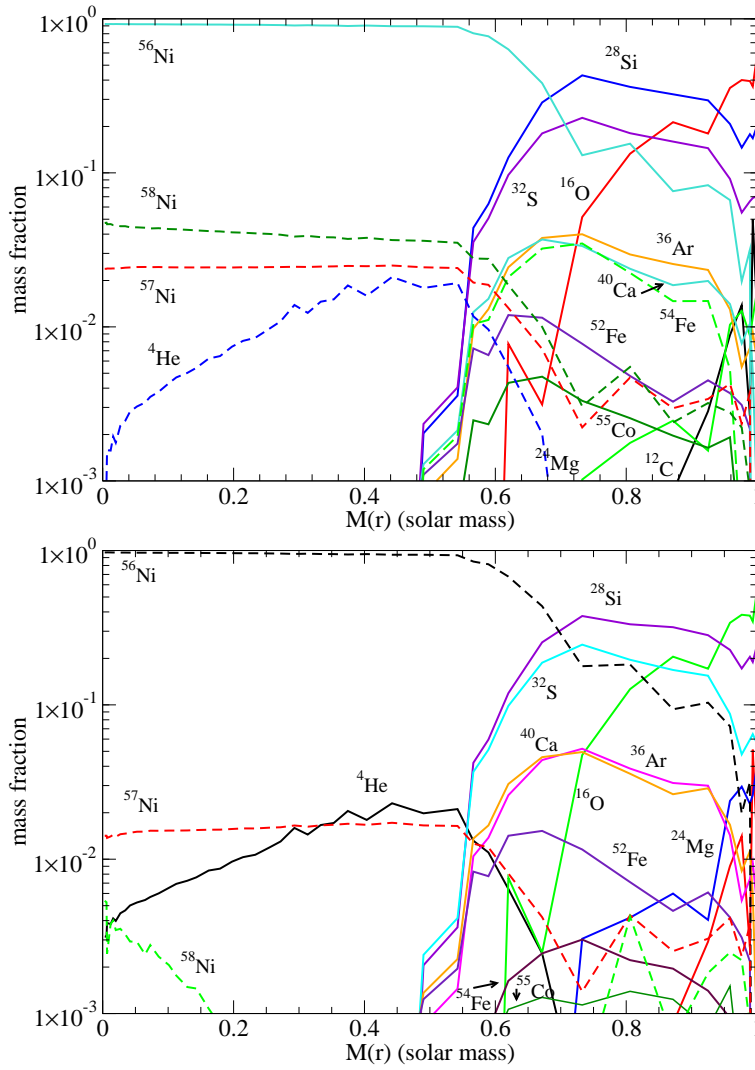


**Fig. 17** Abundance profiles of the sub-Chandrasekhar mass model of  $1.0 M_{\odot}$  as a function of  $M_r$  of the white dwarf.

$Z = Z_{\odot}$  (upper) and the lower metallicity  $Z = 0.1 Z_{\odot}$  (lower). For both models,  $^{56}\text{Ni}$  mass is  $\sim 0.6 M_{\odot}$ .

In the Fe-peak region, some neutron-rich species ( $^{58}\text{Ni}$  and  $^{57}\text{Ni}$ ) are synthesized because initial CNO elements are converted to neutron-rich  $^{22}\text{Ne}$  during He-burning. It is seen that the amount of  $^{58}\text{Ni}$  in the low metallicity model is much smaller than the solar metallicity model.

Figure 18 shows integrated abundances of  $[X_i/^{56}\text{Fe}]$  for both metallicity. Because of the low neutron excess in the central region, there is no overproduction of  $[X_i/^{56}\text{Fe}]$ , in particular,  $^{54}\text{Fe}$ ,  $^{58}\text{Ni}$ , and  $^{64}\text{Cr}$ . In fact, for the solar metallicity

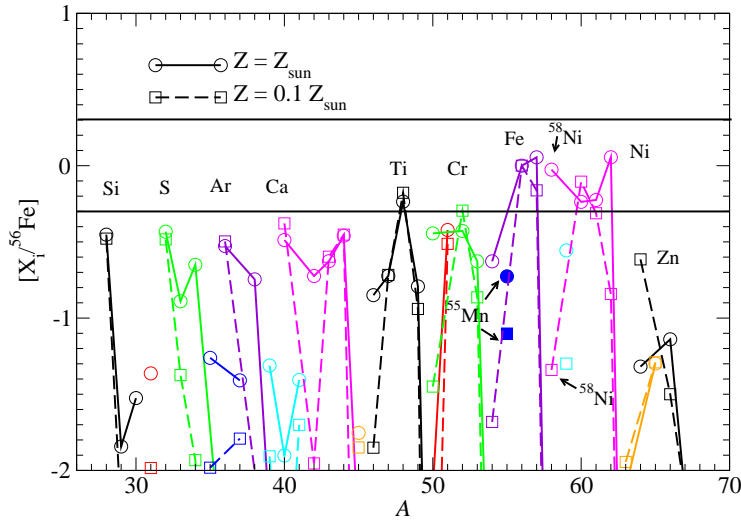


**Fig. 18** The ratios of integrated abundances of the sub-Chandrasekhar mass model of  $1.0 M_{\odot}$  after the decay of unstable nuclei, normalized to  $^{56}\text{Fe}$ , relative to solar abundances. Models with  $Z = Z_{\odot}$  (solid line) and  $0.1 Z_{\odot}$  (dashed line) are used to contrast the effects of metallicity. (*Remark:* The figure is replaced due to the updated table.)

model,  $[^{58}\text{Ni}/^{56}\text{Fe}] \sim 0$ . However, large underproduction is seen in  $[^{55}\text{Mn}/^{56}\text{Fe}]$  for both metallicities and  $[^{58}\text{Ni}/^{56}\text{Fe}]$  for  $Z = 0.1 Z_{\odot}$ . These underproductions are important difference between the Chandrasekhar mass and sub-Chandrasekhar mass models when compared with the observations.

For intermediate mass elements, there are almost no metallicity effects on  $^{28}\text{Si}$ ,  $^{32}\text{S}$ ,  $^{36}\text{Ar}$  and  $^{40}\text{Ca}$ . However, underproduction is seen in slightly neutron-rich isotopes such as  $^{33}\text{S}$ ,  $^{38}\text{Ar}$  and  $^{42}\text{Ca}$  for  $Z = 0.1 Z_{\odot}$ . These species have a closer  $Y_e$  to  $^{22}\text{Ne}$ .

In short, the yields of the sub-Chandrasekhar mass models with the solar metallicity are similar to the Chandrasekhar mass model. The important difference, however, is the Mn yield, which is much smaller in the sub-Chandrasekhar model than the Chandrasekhar mass models. For the smaller metallicity, the differences are larger, so that the comparison with observations of SNe and SNRs in small galaxies is important.

### 6.3 $^{56}\text{Ni}$ Mass as a Function of White Dwarf Mass $M$

It is interesting to know the maximum  $M_{\text{Ni}}$  which can be produced in the explosion of WDs. Figure 19 shows the  $^{56}\text{Ni}$  mass ( $M_{\text{Ni}}$ ) against the white dwarf mass  $M$  for the sub-Chandrasekhar mass models with solar metallicity. The double detonation model is used as the explosion mechanism for the sub-Chandrasekhar mass white dwarfs, i.e., we consider carbon detonation model triggered by spherical helium detonation. Due to the extra degree of freedom for the He envelope in the sub-Chandrasekhar model, models with the minimal He envelope mass sufficient for triggering the carbon detonation are used.



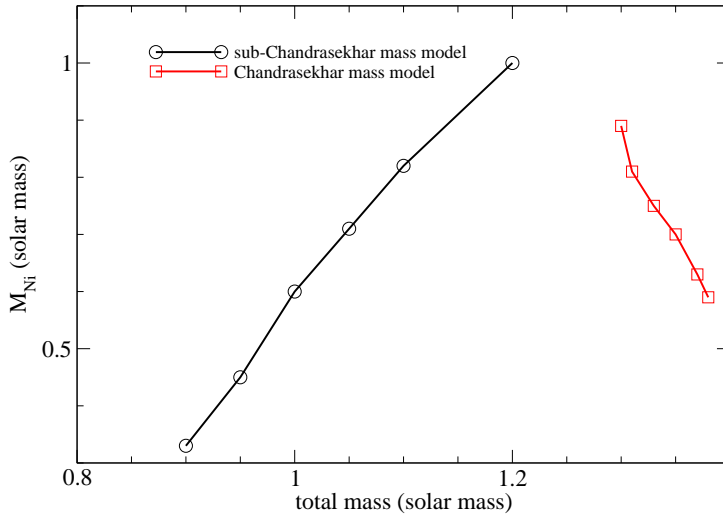


**Fig. 19** The  $^{56}\text{Ni}$  mass against white dwarf mass for the sub-Chandrasekhar mass models and the near-Chandrasekhar mass models. Solar metallicity is assumed for all models shown here. For the sub-Chandrasekhar mass models, the double detonation model, i.e., the He envelope with the minimal mass required to trigger the carbon detonation is used. For Chandrasekhar mass models, the turbulent deflagration model with deflagration-detonation transition is used (Leung and Nomoto 2018).

By symmetry, the spherical shock wave can propagate into the the carbon-oxygen core without significant shock compression in the low density region. As a result, the shock can reach deep in the core where shock convergence can be significant to heat up the core and trigger the carbon detonation.

In the sub-Chandrasekhar mass model sequence,  $M_{\text{Ni}}$  sharply increases with  $M$  for all models. Models with  $M \sim 1M_{\odot}$  gives a typical  $M_{\text{Ni}}$  of  $0.6 M_{\odot}$ . This corresponds to the bare CO mass of about  $0.95 M_{\odot}$ .

There exist two factors that could affect the monotonic increase in  $M_{\text{Ni}}$  with  $M$ . One is the asphericity. The aspherical model always produces less  $^{56}\text{Ni}$  than the spherical because the off-center carbon detonation allows more expansion before the detonation wave sweeps across the whole white dwarf.

The other is the increasing central density with  $M$ . At high central density of the near-Chandrasekhar mass model, the shock wave is too weak to form a detonation, so that a convective deflagration wave is formed as discussed in §6.1.

Figure 19 shows the  $M_{\text{Ni}}$  vs.  $M$  relation for the near-Chandrasekhar mass models. Here the turbulent deflagration model with deflagration-detonation transition (DDT) is used (Leung and Nomoto 2018). There is a monotonic decrease with mass for the Chandrasekhar mass sequence. Since DDT occurs at sufficiently low density, a fraction of the detonation that tends to produce larger  $M_{\text{Ni}}$  than the deflagration is smaller for larger  $M$ . (Even at higher central densities, electron capture suppresses the production of  $^{56}\text{Ni}$ .)

As seen in Figure 19, the maximum  $M_{\text{Ni}}$  depends on at which  $M$ , a deflagration rather than a detonation is formed in the center.

**Table 1** The yield table of the stable isotopes for the W7, WDD2 and the  $1.0 M_{\odot}$  sub-Chandrasekhar mass models with  $Z = Z_{\odot}$  and  $Z = 0.1 Z_{\odot}$ . All short-lived isotopes are assumed to have decayed. All masses are in units of solar mass. (*Remark:* The table is updated and is different from the published version due to previous typos in the tables. )

Isotope	W7	W7	WDD2	Sub-Chand.	Sub-Chand.
Metallicity	$Z_{\odot}$	$0.1 Z_{\odot}$	$Z_{\odot}$	$Z_{\odot}$	$0.1 Z_{\odot}$
<sup>12</sup> C	$5.20 \times 10^{-2}$	$5.44 \times 10^{-2}$	$1.0 \times 10^{-2}$	$1.15 \times 10^{-3}$	$1.17 \times 10^{-3}$
<sup>13</sup> C	$1.81 \times 10^{-11}$	$1.37 \times 10^{-12}$	$2.8 \times 10^{-7}$	$3.2 \times 10^{-9}$	$8.4 \times 10^{-11}$
<sup>14</sup> N	$9.56 \times 10^{-10}$	$8.11 \times 10^{-10}$	$2.0 \times 10^{-7}$	$1.81 \times 10^{-8}$	$1.76 \times 10^{-9}$
<sup>15</sup> N	$1.35 \times 10^{-10}$	$1.41 \times 10^{-8}$	$1.27 \times 10^{-8}$	$2.13 \times 10^{-10}$	$4.93 \times 10^{-9}$
<sup>16</sup> O	$1.85 \times 10^{-1}$	$1.35 \times 10^{-1}$	$9.94 \times 10^{-2}$	$6.64 \times 10^{-2}$	$6.34 \times 10^{-2}$
<sup>17</sup> O	$1.75 \times 10^{-10}$	$1.27 \times 10^{-11}$	$6.88 \times 10^{-8}$	$1.8 \times 10^{-8}$	$2.70 \times 10^{-10}$
<sup>18</sup> O	$7.4 \times 10^{-12}$	$7.45 \times 10^{-13}$	$3.46 \times 10^{-9}$	$9.43 \times 10^{-11}$	$8.33 \times 10^{-12}$
<sup>19</sup> F	$4.54 \times 10^{-12}$	$3.89 \times 10^{-12}$	$4.22 \times 10^{-10}$	$2.39 \times 10^{-11}$	$7.31 \times 10^{-12}$
<sup>20</sup> Ne	$1.62 \times 10^{-3}$	$1.64 \times 10^{-3}$	$1.54 \times 10^{-2}$	$1.15 \times 10^{-3}$	$1.27 \times 10^{-3}$
<sup>21</sup> Ne	$6.97 \times 10^{-8}$	$3.16 \times 10^{-9}$	$2.41 \times 10^{-6}$	$1.57 \times 10^{-7}$	$5.41 \times 10^{-9}$
<sup>22</sup> Ne	$2.73 \times 10^{-3}$	$2.73 \times 10^{-4}$	$1.38 \times 10^{-5}$	$9.25 \times 10^{-9}$	$3.38 \times 10^{-9}$
<sup>23</sup> Na	$6.61 \times 10^{-6}$	$2.56 \times 10^{-6}$	$1.47 \times 10^{-4}$	$8.39 \times 10^{-6}$	$3.86 \times 10^{-6}$
<sup>24</sup> Mg	$4.26 \times 10^{-3}$	$9.74 \times 10^{-3}$	$1.3 \times 10^{-2}$	$1.28 \times 10^{-3}$	$3.10 \times 10^{-3}$
<sup>25</sup> Mg	$1.81 \times 10^{-5}$	$2.78 \times 10^{-6}$	$2.98 \times 10^{-4}$	$1.45 \times 10^{-5}$	$8.53 \times 10^{-7}$
<sup>26</sup> Mg	$2.35 \times 10^{-5}$	$2.96 \times 10^{-6}$	$5.2 \times 10^{-4}$	$2.89 \times 10^{-5}$	$3.45 \times 10^{-6}$
<sup>26</sup> Al	$2.60 \times 10^{-10}$	$5.4 \times 10^{-28}$	$6.9 \times 10^{-9}$	$2.60 \times 10^{-29}$	$2.60 \times 10^{-29}$
<sup>27</sup> Al	$4.50 \times 10^{-4}$	$1.75 \times 10^{-4}$	$1.2 \times 10^{-3}$	$1.14 \times 10^{-4}$	$4.76 \times 10^{-5}$
<sup>28</sup> Si	$1.55 \times 10^{-1}$	$1.43 \times 10^{-1}$	$2.29 \times 10^{-1}$	$1.25 \times 10^{-1}$	$1.18 \times 10^{-1}$
<sup>29</sup> Si	$7.73 \times 10^{-4}$	$1.91 \times 10^{-4}$	$1.31 \times 10^{-3}$	$2.67 \times 10^{-4}$	$9.34 \times 10^{-5}$
<sup>30</sup> Si	$1.64 \times 10^{-3}$	$7.10 \times 10^{-5}$	$1.32 \times 10^{-3}$	$3.79 \times 10^{-4}$	$2.23 \times 10^{-5}$
<sup>31</sup> P	$3.94 \times 10^{-4}$	$5.76 \times 10^{-5}$	$3.4 \times 10^{-4}$	$1.53 \times 10^{-4}$	$2.88 \times 10^{-5}$
<sup>32</sup> S	$7.80 \times 10^{-2}$	$8.29 \times 10^{-2}$	$1.30 \times 10^{-1}$	$6.56 \times 10^{-2}$	$6.89 \times 10^{-2}$
<sup>33</sup> S	$3.77 \times 10^{-4}$	$1.16 \times 10^{-4}$	$2.38 \times 10^{-4}$	$1.89 \times 10^{-4}$	$7.31 \times 10^{-5}$
<sup>34</sup> S	$2.20 \times 10^{-3}$	$1.17 \times 10^{-4}$	$2.46 \times 10^{-3}$	$1.91 \times 10^{-3}$	$1.15 \times 10^{-4}$
<sup>36</sup> S	$2.94 \times 10^{-7}$	$2.25 \times 10^{-9}$	$1.93 \times 10^{-7}$	$6.35 \times 10^{-8}$	$5.80 \times 10^{-10}$
<sup>35</sup> Cl	$1.25 \times 10^{-4}$	$1.73 \times 10^{-5}$	$1.2 \times 10^{-4}$	$1.4 \times 10^{-4}$	$1.80 \times 10^{-5}$
<sup>37</sup> Cl	$2.28 \times 10^{-5}$	$8.36 \times 10^{-6}$	$2.53 \times 10^{-5}$	$2.51 \times 10^{-5}$	$9.59 \times 10^{-6}$
<sup>36</sup> Ar	$1.33 \times 10^{-2}$	$1.77 \times 10^{-2}$	$2.50 \times 10^{-2}$	$1.15 \times 10^{-2}$	$1.41 \times 10^{-2}$
<sup>38</sup> Ar	$8.75 \times 10^{-4}$	$5.15 \times 10^{-5}$	$1.15 \times 10^{-3}$	$1.34 \times 10^{-3}$	$8.62 \times 10^{-5}$
<sup>40</sup> Ar	$7.39 \times 10^{-9}$	$1.55 \times 10^{-11}$	$3.18 \times 10^{-9}$	$1.71 \times 10^{-9}$	$4.26 \times 10^{-12}$
<sup>39</sup> K	$6.57 \times 10^{-5}$	$1.18 \times 10^{-5}$	$6.59 \times 10^{-5}$	$9.25 \times 10^{-5}$	$2.17 \times 10^{-5}$
<sup>40</sup> K	$8.27 \times 10^{-8}$	$2.0 \times 10^{-9}$	$3.17 \times 10^{-8}$	$3.84 \times 10^{-8}$	$1.58 \times 10^{-9}$
<sup>41</sup> K	$4.8 \times 10^{-6}$	$1.45 \times 10^{-6}$	$5.7 \times 10^{-6}$	$5.64 \times 10^{-6}$	$2.71 \times 10^{-6}$
<sup>40</sup> Ca	$1.15 \times 10^{-2}$	$1.74 \times 10^{-2}$	$2.47 \times 10^{-2}$	$1.4 \times 10^{-2}$	$1.40 \times 10^{-2}$
<sup>42</sup> Ca	$2.66 \times 10^{-5}$	$1.49 \times 10^{-6}$	$2.92 \times 10^{-5}$	$4.24 \times 10^{-5}$	$2.58 \times 10^{-6}$
<sup>43</sup> Ca	$1.49 \times 10^{-7}$	$4.70 \times 10^{-8}$	$1.65 \times 10^{-7}$	$1.38 \times 10^{-5}$	$1.36 \times 10^{-5}$
<sup>44</sup> Ca	$9.17 \times 10^{-6}$	$1.42 \times 10^{-5}$	$2.36 \times 10^{-5}$	$2.63 \times 10^{-4}$	$2.76 \times 10^{-4}$
<sup>46</sup> Ca	$3.26 \times 10^{-10}$	$4.35 \times 10^{-11}$	$1.40 \times 10^{-9}$	$4.90 \times 10^{-11}$	$8.14 \times 10^{-16}$
<sup>48</sup> Ca	$2.19 \times 10^{-12}$	$2.9 \times 10^{-12}$	$1.36 \times 10^{-9}$	$9.28 \times 10^{-16}$	$1.61 \times 10^{-22}$
<sup>45</sup> Sc	$2.81 \times 10^{-7}$	$9.74 \times 10^{-8}$	$2.22 \times 10^{-7}$	$3.77 \times 10^{-7}$	$2.72 \times 10^{-7}$
<sup>46</sup> Ti	$1.27 \times 10^{-5}$	$8.69 \times 10^{-7}$	$1.26 \times 10^{-5}$	$1.85 \times 10^{-5}$	$1.70 \times 10^{-6}$
<sup>47</sup> Ti	$5.74 \times 10^{-7}$	$1.39 \times 10^{-7}$	$1.21 \times 10^{-6}$	$2.27 \times 10^{-5}$	$2.18 \times 10^{-5}$
<sup>48</sup> Ti	$2.51 \times 10^{-4}$	$3.66 \times 10^{-4}$	$5.99 \times 10^{-4}$	$7.8 \times 10^{-4}$	$7.82 \times 10^{-4}$
<sup>49</sup> Ti	$2.23 \times 10^{-5}$	$1.53 \times 10^{-5}$	$4.29 \times 10^{-5}$	$1.47 \times 10^{-5}$	$1.2 \times 10^{-5}$
<sup>50</sup> Ti	$9.60 \times 10^{-6}$	$9.33 \times 10^{-6}$	$2.22 \times 10^{-4}$	$6.7 \times 10^{-10}$	$1.58 \times 10^{-13}$
<sup>50</sup> V	$1.84 \times 10^{-8}$	$6.94 \times 10^{-9}$	$1.15 \times 10^{-8}$	$3.68 \times 10^{-9}$	$2.22 \times 10^{-11}$
<sup>51</sup> V	$9.47 \times 10^{-5}$	$5.84 \times 10^{-5}$	$1.41 \times 10^{-4}$	$7.62 \times 10^{-5}$	$5.47 \times 10^{-5}$

**Table 2** (cont'd) The yield table of the stable isotopes for the W7, WDD2 and the  $1.0 M_{\odot}$  sub-Chandrasekhar mass models with  $Z = Z_{\odot}$  and  $Z = 0.1 Z_{\odot}$ . All masses are in units of solar mass. (*Remark:* The table is updated and is different from the published version due to previous typos in the tables. )

Isotope	W7	W7	WDD2	Sub-Chand.	Sub-Chand.
Metallicity	$Z_{\odot}$	$0.1 Z_{\odot}$	$Z_{\odot}$	$Z_{\odot}$	$0.1 Z_{\odot}$
$^{50}\text{Cr}$	$3.74 \times 10^{-4}$	$1.54 \times 10^{-4}$	$3.99 \times 10^{-4}$	$1.41 \times 10^{-4}$	$1.34 \times 10^{-5}$
$^{52}\text{Cr}$	$8.59 \times 10^{-3}$	$1.3 \times 10^{-2}$	$1.54 \times 10^{-2}$	$2.94 \times 10^{-3}$	$3.86 \times 10^{-3}$
$^{53}\text{Cr}$	$1.11 \times 10^{-3}$	$8.73 \times 10^{-4}$	$1.30 \times 10^{-3}$	$2.14 \times 10^{-4}$	$1.21 \times 10^{-4}$
$^{54}\text{Cr}$	$1.30 \times 10^{-4}$	$1.26 \times 10^{-4}$	$1.77 \times 10^{-3}$	$4.40 \times 10^{-8}$	$1.18 \times 10^{-9}$
$^{55}\text{Mn}$	$1.36 \times 10^{-2}$	$1.3 \times 10^{-2}$	$8.21 \times 10^{-3}$	$1.32 \times 10^{-3}$	$5.59 \times 10^{-4}$
$^{54}\text{Fe}$	$1.15 \times 10^{-1}$	$8.82 \times 10^{-2}$	$6.98 \times 10^{-2}$	$8.69 \times 10^{-3}$	$8.14 \times 10^{-4}$
$^{56}\text{Fe}$	$6.68 \times 10^{-1}$	$7.24 \times 10^{-1}$	$6.54 \times 10^{-1}$	$6.0 \times 10^{-1}$	$6.38 \times 10^{-1}$
$^{57}\text{Fe}$	$1.96 \times 10^{-2}$	$1.51 \times 10^{-2}$	$1.34 \times 10^{-2}$	$1.60 \times 10^{-2}$	$1.6 \times 10^{-2}$
$^{58}\text{Fe}$	$5.46 \times 10^{-4}$	$5.32 \times 10^{-4}$	$4.70 \times 10^{-3}$	$1.36 \times 10^{-8}$	$1.86 \times 10^{-9}$
$^{60}\text{Fe}$	$7.33 \times 10^{-10}$	$6.97 \times 10^{-10}$	$4.10 \times 10^{-8}$	$3.4 \times 10^{-18}$	$1.81 \times 10^{-21}$
$^{59}\text{Co}$	$5.20 \times 10^{-4}$	$4.29 \times 10^{-4}$	$3.92 \times 10^{-4}$	$5.27 \times 10^{-4}$	$9.1 \times 10^{-5}$
$^{58}\text{Ni}$	$6.80 \times 10^{-2}$	$4.71 \times 10^{-2}$	$3.0 \times 10^{-2}$	$2.50 \times 10^{-2}$	$1.18 \times 10^{-3}$
$^{60}\text{Ni}$	$4.51 \times 10^{-3}$	$5.39 \times 10^{-3}$	$6.82 \times 10^{-3}$	$6.13 \times 10^{-3}$	$8.14 \times 10^{-3}$
$^{61}\text{Ni}$	$5.81 \times 10^{-5}$	$5.77 \times 10^{-5}$	$2.35 \times 10^{-4}$	$2.78 \times 10^{-4}$	$2.33 \times 10^{-4}$
$^{62}\text{Ni}$	$7.3 \times 10^{-4}$	$3.83 \times 10^{-4}$	$3.5 \times 10^{-3}$	$1.72 \times 10^{-3}$	$2.15 \times 10^{-4}$
$^{64}\text{Ni}$	$4.17 \times 10^{-7}$	$4.6 \times 10^{-7}$	$1.70 \times 10^{-5}$	$4.59 \times 10^{-14}$	$3.79 \times 10^{-14}$
$^{63}\text{Cu}$	$5.15 \times 10^{-7}$	$3.57 \times 10^{-7}$	$1.69 \times 10^{-6}$	$2.50 \times 10^{-6}$	$3.69 \times 10^{-6}$
$^{65}\text{Cu}$	$1.96 \times 10^{-7}$	$1.96 \times 10^{-7}$	$1.3 \times 10^{-6}$	$7.61 \times 10^{-6}$	$7.68 \times 10^{-6}$
$^{64}\text{Zn}$	$1.34 \times 10^{-6}$	$4.20 \times 10^{-6}$	$1.96 \times 10^{-5}$	$2.70 \times 10^{-5}$	$1.31 \times 10^{-4}$
$^{66}\text{Zn}$	$3.42 \times 10^{-6}$	$1.14 \times 10^{-6}$	$3.12 \times 10^{-5}$	$2.41 \times 10^{-5}$	$1.1 \times 10^{-5}$
$^{67}\text{Zn}$	$2.28 \times 10^{-9}$	$4.24 \times 10^{-10}$	$1.90 \times 10^{-8}$	$3.41 \times 10^{-7}$	$3.33 \times 10^{-7}$
$^{68}\text{Zn}$	$1.29 \times 10^{-9}$	$2.95 \times 10^{-9}$	$1.61 \times 10^{-8}$	$3.71 \times 10^{-7}$	$6.8 \times 10^{-7}$
$^{70}\text{Zn}$	$2.93 \times 10^{-14}$	$2.85 \times 10^{-14}$	$1.29 \times 10^{-11}$	$1.97 \times 10^{-18}$	$1.48 \times 10^{-18}$

**Table 3** The yield table of the radioactive isotopes for the W7, WDD2 and the  $1.0 M_{\odot}$  sub-Chandrasekhar mass models with  $Z = Z_{\odot}$  and  $Z = 0.1 Z_{\odot}$ . All masses are in units of solar mass. (*Remark:* The table is updated and is different from the published version due to previous typos in the tables.)

Isotope	W7	W7	WDD2	Sub-Chand.	Sub-Chand.
Metallicity	$Z_{\odot}$	$0.1 Z_{\odot}$	$Z_{\odot}$	$Z_{\odot}$	$0.1 Z_{\odot}$
$^{22}\text{Na}$	$4.89 \times 10^{-9}$	$2.89 \times 10^{-9}$	$6.20 \times 10^{-8}$	$3.74 \times 10^{-9}$	$3.22 \times 10^{-9}$
$^{26}\text{Al}$	$2.23 \times 10^{-6}$	$1.66 \times 10^{-6}$	$2.84 \times 10^{-5}$	$1.70 \times 10^{-6}$	$1.74 \times 10^{-6}$
$^{39}\text{Ar}$	$1.71 \times 10^{-8}$	$2.20 \times 10^{-10}$	$6.11 \times 10^{-9}$	$7.27 \times 10^{-9}$	$1.11 \times 10^{-10}$
$^{40}\text{K}$	$8.32 \times 10^{-8}$	$2.1 \times 10^{-9}$	$3.19 \times 10^{-8}$	$3.86 \times 10^{-8}$	$1.59 \times 10^{-9}$
$^{41}\text{Ca}$	$4.5 \times 10^{-6}$	$1.47 \times 10^{-6}$	$4.99 \times 10^{-6}$	$5.66 \times 10^{-6}$	$2.38 \times 10^{-6}$
$^{44}\text{Ti}$	$8.48 \times 10^{-6}$	$1.33 \times 10^{-5}$	$2.21 \times 10^{-5}$	$2.64 \times 10^{-4}$	$2.68 \times 10^{-4}$
$^{48}\text{V}$	$4.24 \times 10^{-8}$	$1.21 \times 10^{-8}$	$6.88 \times 10^{-8}$	$1.96 \times 10^{-7}$	$1.47 \times 10^{-7}$
$^{49}\text{V}$	$2.21 \times 10^{-7}$	$3.59 \times 10^{-8}$	$1.25 \times 10^{-7}$	$1.54 \times 10^{-7}$	$1.18 \times 10^{-8}$
$^{53}\text{Mn}$	$1.97 \times 10^{-4}$	$1.75 \times 10^{-4}$	$1.44 \times 10^{-4}$	$9.5 \times 10^{-6}$	$4.27 \times 10^{-7}$
$^{60}\text{Fe}$	$1.2 \times 10^{-8}$	$9.99 \times 10^{-9}$	$5.73 \times 10^{-7}$	$4.59 \times 10^{-17}$	$2.90 \times 10^{-20}$
$^{56}\text{Co}$	$1.8 \times 10^{-4}$	$8.97 \times 10^{-5}$	$5.60 \times 10^{-5}$	$8.93 \times 10^{-6}$	$5.89 \times 10^{-6}$
$^{57}\text{Co}$	$7.65 \times 10^{-4}$	$7.32 \times 10^{-4}$	$3.48 \times 10^{-4}$	$5.62 \times 10^{-6}$	$1.23 \times 10^{-6}$
$^{60}\text{Co}$	$7.72 \times 10^{-8}$	$7.49 \times 10^{-8}$	$3.52 \times 10^{-7}$	$1.17 \times 10^{-13}$	$7.99 \times 10^{-15}$
$^{56}\text{Ni}$	$6.45 \times 10^{-1}$	$7.2 \times 10^{-1}$	$6.32 \times 10^{-1}$	$6.0 \times 10^{-1}$	$6.38 \times 10^{-1}$
$^{57}\text{Ni}$	$1.88 \times 10^{-2}$	$1.42 \times 10^{-2}$	$1.28 \times 10^{-2}$	$1.60 \times 10^{-2}$	$1.6 \times 10^{-2}$
$^{59}\text{Ni}$	$3.3 \times 10^{-4}$	$2.86 \times 10^{-4}$	$1.1 \times 10^{-4}$	$2.89 \times 10^{-6}$	$1.61 \times 10^{-6}$
$^{63}\text{Ni}$	$8.47 \times 10^{-8}$	$8.26 \times 10^{-8}$	$8.17 \times 10^{-7}$	$2.12 \times 10^{-15}$	$9.34 \times 10^{-16}$

## 7 Summary

In this review, we review how the single degenerate models for Type Ia supernovae (SNe Ia) work. In this binary system, the white dwarf (WD) accretes either hydrogen-rich matter or helium and undergoes hydrogen and helium shell-burning from its non-degenerate companion star. We summarize how the stability and non-linear behavior of such shell-burning depend on the accretion rate and the WD mass and how the WD blows strong wind.

We identify the following evolutionary routes for the accreting WD to trigger a thermonuclear explosion. Typically, the accretion rate is quite high in the early stage and gradually decreases as a result of mass transfer. With decreasing rate, the WD evolves as follows:

(1) At a rapid accretion phase, the WD increase its mass by stable H burning and blows a strong wind to keep its moderate radius. The wind is strong enough to strip a part of the companion star's envelope to control the accretion rate and forms circumstellar matter (CSM). If the WD explodes within CSM, it is observed as an "SN Ia-CSM". (X-rays emitted by the WD are absorbed by CSM.)

(2) If the WD continues to accrete at a lower rate, the wind stops and an SN Ia is triggered under steady-stable H shell-burning, which is observed as a super-soft X-ray source: "SN Ia-SXSS".

(3) If the accretion continues at a still lower rate, H shell-burning becomes unstable and many flashes recur. The WD undergoes recurrent nova (RN) whose mass ejection is smaller than the accreted matter. Then the WD evolves to an "SN Ia-RN".

(4) If the companion is a He star (or a He WD), the accretion of He can trigger He and C double detonations at the sub-Chandrasekhar mass or the WD grows to the Chandrasekhar mass under a He-wind: "SN Ia-He CSM".

(5) If the accreting WD rotates quite rapidly, the WD mass can exceed the Chandrasekhar mass of the spherical WD, which delays the trigger of an SN Ia. After angular momentum is lost from the WD, the (super-Chandra) WD contracts to become a delayed SN Ia. The companion star has become a He WD and CSM has disappeared: "SN Ia-He WD".

Finally, we update nucleosynthesis yields of the carbon deflagration model W7, delayed detonation model WDD2, and the sub-Chandrasekhar mass model to provide some constraints on the yields (such as Mn) from the comparison with the observations. We note the important metallicity effects on  $^{58}\text{Ni}$  and  $^{55}\text{Mn}$ .

**Acknowledgements** This work has been supported by the World Premier International Research Center Initiative (WPI Initiative), MEXT, Japan, and JSPS KAKENHI Grant Numbers JP26400222, JP16H02168, JP17K05382.

## References

- Arnett, D.: A Possible Model of Supernovae: Detonation of  $^{12}\text{C}$ . *Ap & SS* **5**, 180 (1969)
- Arnett, D.: *Supernovae and Nucleosynthesis*. *Supernovae and Nucleosynthesis* (Princeton University Press) (1996)
- Benvenuto, O. G., Panei, J. A., Nomoto, K., Kitamura, H., Hachisu, I.: Final Evolution and Delayed Explosions of Spinning White Dwarfs in Single Degenerate Models for Type Ia Supernovae. *ApJL* **809**, L6 (2015)

- Dilday, B., Howell, D. A., Cenko, S. B., et al.: PTF 11kx: A Type Ia Supernova with a Symbiotic Nova Progenitor. *Science* **337**, 942 (2012)
- Di Stefano, R., Voss, R., Claeys, J. S. W.: Spin-up/Spin-down Models for Type Ia Supernovae. *ApJL* **738**, L1 (2011)
- Foley, R. J., Simon, J. D., Burns, C. R., et al.: Linking Type Ia Supernova Progenitors and Their Resulting Explosions. *ApJ* **752**, 101 (2012)
- Fujimoto, M.-Y., Sugimoto, D.: Helium shell flashes and evolution of accreting white dwarfs. *ApJ* **257**, 291 (1982)
- Fuller, G., Fowler, W., Newman, M.: Stellar weak interaction rates for intermediate mass nuclei. III - Rate tables for the free nucleons and nuclei with  $A = 21$  to  $A = 60$ . *ApJS* **48**, 279 (1982)
- Hachisu, I., Kato, M., Nomoto, K.: A New Model for Progenitor Systems of Type Ia Supernovae. *ApJL* **470**, 97 (1996)
- Hachisu, I., Kato, M., Nomoto, K., Umeda, H.: A New Evolutionary Path to Type IA Supernovae: A Helium-rich Supersoft X-Ray Source Channel. *ApJ* **519**, 314 (1999)
- Hachisu, I., Kato, M., Nomoto, K.: A Wide Symbiotic Channel to Type IA Supernovae. *ApJ* **522**, 487 (1999)
- Hachisu, I., Kato, M., & Nomoto, K.: Young and Massive Binary Progenitors of Type Ia Supernovae and Their Circumstellar Matter. *ApJ* **679**, 1390-1404 (2008a)
- Hachisu, I., Kato, M., & Nomoto, K.: The Delay-Time Distribution of Type Ia Supernovae and the Single-Degenerate Model. *ApJ* **683**, L27 (2008b)
- Hachisu, I., Kato, M., Nomoto, K.: Final Fates of Rotating White Dwarfs and Their Companions in the Single Degenerate Model of Type Ia Supernovae. *ApJL* **756**, L4 (2012)
- Hachisu, I., Kato, M., Saio, H., Nomoto, K.: A Single Degenerate Progenitor Model for Type Ia Supernovae Highly Exceeding the Chandrasekhar Mass Limit. *ApJ* **744**, 69 (2012)
- Hashimoto, M., Nomoto, K., Arai, K., Kaminishi, K.: The  $(^{14}\text{N})(e^-, \nu)(^{14}\text{C})(\alpha, \gamma)(^{18}\text{O})$  reaction and helium flashes in accreting helium white dwarfs. *ApJ* **307**, 687 (1986)
- Hamuy, M., Phillips, M. M., Suntzeff, N. B., et al.: An asymptotic-giant-branch star in the progenitor system of a type Ia supernova. *Nature* **424**, 651 (2003)
- Han, Z., Podsiadlowski, Ph.: The single-degenerate channel for the progenitors of Type Ia supernovae. *MNRAS* **350**, 1301 (2004)
- Hillebrandt, W., Niemeyer, J. C.: Type Ia Supernova Explosion Models. *ARAAS* **38**, 191 (2000)
- Iben, I., Jr., Tutukov, A. V.: Supernovae of type I as end products of the evolution of binaries with components of moderate initial mass ( $M$  not greater than about 9 solar masses). *ApJS* **54**, 335 (1984).
- Iben, I., Jr., Nomoto, K., Tornambe, A., Tutukov, A. V.: On interacting helium star-white dwarf pairs as supernova precursors. *ApJ* **317**, 717 (1987).
- Ilkov, M., Soker, N.: Type Ia supernovae from very long delayed explosion of core-white dwarf merger. *MNRAS* **419**, 1695 (2012)
- Iwamoto, K., Brachwitz, F., Nomoto, K. et al.: Nucleosynthesis in Chandrasekhar Mass Models for Type IA Supernovae and Constraints on Progenitor Systems and Burning-Front Propagation. *ApJS* **125**, 439 (1999).
- Justham, S., Single-degenerate Type Ia Supernovae Without Hydrogen Contamination. *ApJL* **730**, L34 (2011)
- Kamiya, Y., Tanaka, M., Nomoto, K., et al.: Super-Chandrasekhar-mass Light Curve Models for the Highly Luminous Type Ia Supernova 2009dc. *ApJ* **756**, 191 (2012)
- Kato, M., Saio, H., Hachisu, I., Nomoto, K.: Shortest Recurrence Periods of Novae. *ApJ* **793**, 136 (2014)
- Kato, M., Hachisu, I., Saio, H.: Recurrent novae and long-term evolution of mass-accreting white dwarfs – toward the accurate mass retention efficiency. *arXiv:1711.01529* (2017)
- Kawai, Y., Saio, H., Nomoto, K.: Off-center ignition of nuclear burning in merging white dwarfs. *ApJ* **315**, 229 (1987)
- Kawai, Y., Saio, H., Nomoto, K.: Steady state models of white dwarfs accreting helium or carbon/oxygen-rich matter. *ApJ* **315**, 229 (1988)
- Khokhlov, A.: Mechanisms for the initiation of detonations in the degenerate matter of supernovae. *A&A* **245**, 114 (1991)
- Kitamura, H.: Pycnonuclear Reactions in Dense Matter near Solidification. *ApJ* **539**, 888 (2000)
- Langer, N., Deutschmann, A., Wellstein, S., Höflich, P.: The evolution of main sequence star + white dwarf binary systems towards Type Ia supernovae. *A&A* **362**, 1046 (2000)

- Langanke, K., Martinez-Pinedo, G.: Rate Tables for the Weak Processes of pf-SHELL Nuclei in Stellar Environments. *ADNDT* **79**, 1 (2001)
- Leung, S.-C., Chu, M.-C., Lin, L.-M.: A new hydrodynamics code for Type Ia supernovae. *MNRAS* **454**, 1238 (2015a)
- Leung, S.-C., Chu, M.-C., Lin, L.-M.: Dark matter admixed Type Ia supernovae. *ApJ* **812**, 110 (2015b)
- Leung, S.-C., Nomoto, K.: Explosive Nucleosynthesis in Near-Chandrasekhar Mass White Dwarf Models for Type Ia supernovae: Dependence of nucleosynthesis on Model Parameters of Type Ia supernovae. *ApJS* in press (2018) arXiv:1710.04254
- Li, W., Bloom, J. S., Podsiadlowski, P. et al.: Exclusion of a luminous red giant as a companion star to the progenitor of supernova SN 2011fe. *Nature* **480**, 348 (2011)
- Li, X.-D., van den Heuvel, E. P. J.: Evolution of white dwarf binaries: supersoft X-ray sources and progenitors of type IA supernovae. *A&A* **322**, L9 (1997)
- Limongi, M., Tornambe, A.: He stars and He-accreting CO white dwarfs. *ApJ* **371**, 317 (1991)
- Livio, M.: The Progenitors of Type Ia Supernovae. In: *Type Ia Supernovae, Theory and Cosmology*, ed. J.C. Niemeyer, and J.W. Truran (Cambridge: Cambridge University Press) p.33 (2000)
- Livne, E.: Successive detonations in accreting white dwarfs as an alternative mechanism for type I supernovae. *ApJL* **354**, L53 (1990)
- Livne, E., Glasner, A.S.: Numerical simulations of off-center detonations in helium shells. *ApJ* **370**, 272 (1991)
- Mori, K., et al.: Impact of New Gamow-Teller Strengths on Explosive Type Ia Supernova Nucleosynthesis. *ApJ* **833**, 179 (2016)
- Maoz, D., Mannucci, F., Nelemans, G.: Observational Clues to the Progenitors of Type Ia Supernovae. *ARAA* **52**, 107 (2014)
- Nariai, K., Nomoto, K., Sugimoto, D.: Nova Explosion of Mass-Accreting White Dwarfs. *PASJ* **32**, 473 (1980)
- Nomoto, K., Sugimoto, D., Neo, S.: Carbon deflagration supernova, an alternative to carbon detonation. *Ap & SS* **39**, L37 (1976)
- Nomoto, K., Sugimoto, D.: Rejuvenation of Helium White Dwarfs by Mass Accretion. *PASJ* **31**, 287 (1977)
- Nomoto, K., Nariai, K., Sugimoto, D.: Rapid Mass Accretion onto White Dwarfs and Formation of an Extended Envelope. *PASJ* **31**, 287 (1979)
- Nomoto, K.: Accreting white dwarf models for type I supernovae. I - Presupernova evolution and triggering mechanisms. *ApJ* **253**, 798 (1982)
- Nomoto, K.: Accreting white dwarf models for type 1 supernovae. II - Off-center detonation supernovae. *ApJ* **257**, 780 (1982)
- Nomoto, K., Thielemann, F.-K., Yokoi, K.: Accreting white dwarf models of Type I supernovae. III - Carbon deflagration supernovae. *ApJ* **286**, 644 (1984)
- Nomoto, K., Iben, I.-Jr.: Carbon ignition in a rapidly accreting degenerate dwarf - A clue to the nature of the merging process in close binaries. *ApJ* **297**, 531 (1985)
- Nomoto, K., Kondo, Y.: Conditions for accretion-induced collapse of white dwarfs. *ApJL* **367**, 19 (1991)
- Nomoto, K., Yamaoka, H., Shigeyama, T., Kumagai, S., Tsujimoto, T.: Type I supernovae and evolution of interacting binaries. In: *Supernovae*, NATO ASI Ser. C, Proc. of Session LIV held in Les Houche 1990, ed. S. Bludmann et al. (North-Holland) p.199 (1994) <sup>1</sup>
- Nomoto, K., Iwamoto, K., Kishimoto, N.: Type Ia supernovae: their origin and possible applications in cosmology. *Science* **276**, 1378 (1997)
- Nomoto, K., Umeda, H., Kobayashi, C., et al.: Type Ia supernova progenitors, environmental effects, and cosmic supernova rates. In: Niemeyer JC and Truran JW (eds) *Type Ia Supernovae, Theory and Cosmology*, Cambridge University Press, p.63 (2000a)
- Nomoto, K., Umeda, H., Kobayashi, C., et al.: Type Ia supernovae: Progenitors and evolution with redshift. In: *Cosmic Explosions: AIP Conference Proceedings* **522**, 35 (2000b)
- Nomoto, K., Suzuki, T., Deng, J., Uenishi, T., Hachisu, I., Mazzali, P.: Circumstellar Interaction of Type Ia Supernova SN 2002ic. *Frontier in Astroparticle Physics and Cosmology: RESCEU International Symposium Series* **6**, 323 (2004)
- Nomoto, K., Suzuki, T., Deng, J., Uenishi, T., Hachisu, I.: Progenitors of Type Ia Supernovae: Circumstellar Interaction, Rotation, and Steady Hydrogen Burning. In: *Supernovae as*

<sup>1</sup> <http://supernova.astron.s.u-tokyo.ac.jp/~nomoto/reference>

- Cosmological Lighthouses 1604-2004, eds. Turatto et al, ASP Conference Series **342**, 105 (2005)
- Nomoto, K., Saio, H., Kato, M., Hachisu, I.: Thermal Stability of White Dwarfs Accreting Hydrogen-rich Matter and Progenitors of Type Ia Supernovae. *ApJ* **663**, 1269 (2007)
- Nomoto, K., Kamiya, Y., Nakasato, N. et al.: Progenitors of Type Ia Supernovae: Single Degenerate and Double Degenerates. *AIPC* **1111**, 267 (2009).
- Nomoto, K., Kamiya, M., Nakasato, N.: Type Ia Supernova Models and Progenitor Scenarios. In: *IAU Symposium 281, Binary Paths to Type Ia Supernovae Explosions* (Cambridge University Press: Cambridge) p. 253 (2013)
- Nomoto, K., Kobayashi, C., Tominaga, N.: Supernova Explosions of Super-asymptotic Giant Branch Stars: Multicolor Light Curves of Electron-capture Supernovae. *ARAA* **51**, 457 (2013) <sup>1</sup>
- Nomoto, K., Leung, S.-C.: Thermonuclear Explosions of Chandrasekhar Mass White Dwarfs. In: *Handbook of Supernovae*, eds. A.W. Alsabti & P. Murdin (Springer) **2**, 1275 (2017) <sup>1</sup>
- Pakmor, R., Hachinger, S., Röpke, F. K., Hillebrandt, W.: Violent mergers of nearly equal-mass white dwarf as progenitors of subluminous Type Ia supernovae. *A&A* **528**, A117 (2011)
- Patat, F., Chandra, P., Chevalier, R., et al.: Detection of Circumstellar Material in a Normal Type Ia Supernova. *Science* **317**, 924 (2007)
- Piersanti, L., Gagliardi S., Iben I., Tornambe, A.: Carbon-Oxygen White Dwarf Accreting CO-Rich Matter. II. Self-Regulating Accretion Process up to the Explosive Stage. *ApJ* **598**, 1229 (2003)
- Potekhin, A. Y., Chabrier, G.: Thermonuclear fusion in dense stars. Electron screening, conductive cooling, and magnetic field effects. *Astron. & Astropart.* **538**, AA115 (2012)
- Saio, H., Nomoto, K.: Off-Center Carbon Ignition in Rapidly Rotating, Accreting Carbon-Oxygen White Dwarfs. *ApJ* **615**, 444 (2004)
- Sato, Y., Nakasato, N., Tanikawa, A., Nomoto, K., Maedak, K., Hachisu, I.: The Critical Mass Ratio of Double White Dwarf Binaries for Violent Merger-induced Type Ia Supernova Explosions. *ApJ* **821**, 67 (2016)
- Sato, Y., Nakasato, N., Tanikawa, A., Nomoto, K., Maedak, K., Hachisu, I.: The Critical Mass Ratio of Double White Dwarf Binaries for Violent Merger-induced Type Ia Supernova Explosions. *ApJ* **821**, 67 (2017)
- Schaefer, B. E., Pagnotta, A.: An absence of ex-companion stars in the type Ia supernova remnant SNR 0509-67.5. *Nature* **481**, 164 (2012)
- Seitenzahl, I. R., Meakin, C. A., Townsley, D. M., Lamb, D. Q., & Truran, J. W.: Spontaneous Initiation of Detonations in White Dwarf Environments: Determination of Critical Sizes. *ApJ* **696**, 515 (2009)
- Shen, K., & Bildsten, L.: Thermally Stable Nuclear Burning on Accreting White Dwarfs. *ApJ* **660**, 1444 (2007)
- Shigeyama, T., Nomoto, K., Yamoka, H., Thielemann, F.-K.: Possible models for the type IA supernova 1990N. *ApJL* **386**, L13 (1992)
- Starrfield, S., Sparks, W.M., Truran, J.W., Shaviv, G.: Neon Novae Recurrent Novae and Type-I Supernovae. In: *Supernovae*, ed. S.E. Woosley (Springer: Berlin) p. 602 (1991)
- Sternberg, A., Gal-Yam, A., Simon, J. D., et al.: Circumstellar Material in Type Ia Supernovae via Sodium Absorption Features. *Science* **333**, 856 (2011)
- Sugimoto, D., Fujimoto, M.: A General Theory for Thermal Pulses of Finite Amplitude in Nuclear Shell- Burnings. *PASJ* **30**, 467 (1978)
- Sugimoto, D., Fujimoto, M., Nariai, K., Nomoto, K.: In: *IAU Colloquium 53, White Dwarfs and Variable Degenerate Stars*, ed. H.M. Van Horn and V. Weidemann (Univ. of Rochester), p. 280 (1979)
- Sugimoto, D., Nomoto, K.: Presupernova models and supernovae. *Space Sci. Rev.*, **25**, 155 (1980)
- Taam, R.E.: Helium runaways in white dwarfs. *ApJ* **237**, 142 (1980)
- Thielemann, F.-K., Nomoto, K., Yokoi, K.: Explosive nucleosynthesis in carbon deflagration models of Type I supernovae *A & A* **158**, 17 (1986)
- Yield Table: <http://supernova.astron.s.u-tokyo.ac.jp/~nomoto/yields> (2018)
- Webbink, R. F.: Double white dwarfs as progenitors of R Coronae Borealis stars and Type I supernovae. *ApJ* **277**, 355 (1984)
- Woosley, S.E., Taam, R.E., Weaver, T.A.: Models for Type I supernova. I - Detonations in white dwarfs. *ApJ* **301**, 601 (1986)

- Woosley, S.E, Weaver, T.A.: Sub-Chandrasekhar mass models for Type IA supernovae. *ApJ* **423**, 371 (1994)
- Yoon, S. C., Podsiadlowski, P., Rosswog, S.: Remnant evolution after a carbon-oxygen white dwarf merger. *MNRAS* **380**, 933 (2007)